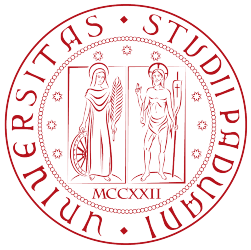

UNIVERSITÀ DEGLI STUDI DI PADOVA

Dipartimento di Fisica e Astronomia "Galileo Galilei"

Master Degree in Physics

Final Dissertation

Motion control of water droplets by means of optical patterns imprinted on Fe:$LiNbO_3$ crystals

Thesis supervisor
Prof. Giampaolo Mistura
Thesis co-supervisor
Dr. Annamaria Zaltron

Candidate
Alessio Meggiolaro

Academic Year 2019/2020

Abstract

Chemical and morphological surface patterning is very common in microfluidic devices to control the flow. In this project, the dynamics of water droplets moving on a iron-doped lithium niobate (Fe:$LiNbO_3$) crystal which has been exposed to optical patterns produced by lenses will be studied. This optowetting technique will exploit the photovoltaic effect of lithium niobate, that creates surface charges upon illumination and enables the control of droplets without fixed electrodes. To reduce the friction, the crystal surfaces will be covered with a micrometric lubricant film (LIS) made of octadecyltrichlorosilane (OTS) impregnated with silicone oil that acts as hydrophobic dielectric layer. The behaviour of the LIS will be investigated by droplet sliding on glass and Fe:$LiNbO_3$ substrates and compared with results from literature. The interaction between charged regions at the Fe:$LiNbO_3$ surface and water will be proved by analyzing pendant droplets falling on the substrates due to the dielectrophoretic force. In the final experiments, the motion of drops with different volumes on straight lines with different inclinations imprinted on samples tilted at different angles will be observed by means of video recordings.

Contents

List of Figures

Introduction

Microfluidics [1, 2] is the science and technology of systems that process and manipulate small droplets, with volumes from μl to a few pl. Since the 1990s, great developments have been done in microfabrication to obtain portable devices in the micrometric scale (the so-called *Lab-on-a-chip*) that permit to synthesize, analyze and transport fluids.
Small quantities of samples and reagents required for the applications, short times for analysis and low cost are specific advantages of this kind of devices. They can be produced in a *closed* configuration, by creating microchannels confined in a matrix, or have an *open* configuration. This latter is preferable because, in principle, it is simpler.

Inspirations from natural structures, such as the leaves of lotus or carnivorous plants, have led to the development of biomimetic surfaces. Suitable engineered surface chemistry and roughness induce remarkable non-wetting properties that enable a passive control of fluids useful for several commercial and technological applications [3, 4]. These features can be obtained by photolithography techniques or chemical functionalizations. However, the suspension of droplets on the tips of these textured surfaces is not stable. For this reason, porous surfaces are impregnated with a lubricant oil, forming *Liquid-Infused Surface(s)* (*LIS*), which guarantee lyophobicity and low adhesion essential to guarantee passive control, mixing and merging of drops.

The modulation of the wetting properties of a substrate can be actively controlled by the *electrowetting* (*EW*) technique [5]. This method permits to direct polar droplets on the substrate by using electrodes that create electric charges on the surface that change its wettability. In such a way many physical phenomena, such as dielectrophoresis (DEP) or electro-osmosis, can be investigated and employed for practical applications. In EW, the electrical double layer formed between the metallic electrode and the electrolyte permits to control the wettability. By adding a thin dielectric film between the liquid and the conducting substrate, the variation of electric energy takes place across the dielectric and the electrolysis at the metallic surface is prevented. This *electrowetting on dielectric* (*EWOD*) method is ideally applicable to any acqueous liquid. The role of the dielectric layer can be played by the LIS, that imparts a complete reversibility and switchability, given by the negligible contact line pinning at the droplet-oil interface (*electrowetting on liquid-infused film, EWOLF* technique [6]). However, in this configuration the microfluidic chip is composed of fixed metallic electrodes used to apply the electric fields whose pattern cannot be modified unless adding new electrodes and removing the old ones from the implemented structure.

To overcome this limitation, optically-induced electrodes can be used, exploiting the *optowetting* (*OW*) technique [7]. In this method, virtual electrodes are generated by simply illuminating a suitable material with the desired light pattern, where strong charge accumulations and electric fields arise. Beside the fact that the preparation of such devices is cheaper and less time-consuming, the main advantage of the OW technique is represented by high degree of reconfigurability of its light-induced electrodes.
A promising candidate for realizing these chips is lithium niobate ($LiNbO_3$), which can be ex-

ploited for its photovoltaic (PV) property that generates high electrostatic evanescent fields by visible illumination of the surface [8]. This material has been used for experiments that relies on its optical, piezoelectric and pyroelectric properties and it has been already proposed for manipulation of cells and nano-objects. The photovoltaic effect consists in the creation of an electric current of free carriers inside the crystal upon the exposure of light with proper wavelength. The photo-excited charge carriers move along a preferred crystallographic direction, producing an accumulation at the surface of the illuminated crystal and, consequently, an external electric field. This effect can be enhanced by doping the material with iron (Fe:$LiNbO_3$), that presents ions in two valence states Fe^{2+} and Fe^{3+}, providing the formation of donors and acceptors for charge carriers [9]. The addition of Fe ions permits to increase photovoltaic fields up to 10^6 V/m and to control the time constant typical for the carriers' separation, dependent on the reduction degree, defined as the ratio Fe^{2+}/Fe^{3+}.

This thesis work has the main goal of controlling droplets' motion by using the novel optowetting method previously presented. Lithium niobate is the medium by which a distribution of free charges is formed on the surface, through the photovoltaic effect. The LIS acts as dielectric hydrophobic layer and it is made of octadecyltrichlorosilane (OTS), an amphiphilic molecule chemically deposited on Fe:$LiNbO_3$ samples, and impregnated with silicone oil. The illumination of the crystals is provided by a diode-pumped laser; the gaussian laser beam can be shaped into a stripe along one direction through a cylindrical lens to create different line-shaped paths. The behaviour of sliding droplets on LIS is tested for different volumes and tilting angles of the substrate and compared with literature. The interaction between charged regions at the Fe:$LiNbO_3$ surface and water micro-droplets is investigated by analyzing the behaviour of pendant droplets falling on the substrates due to dielectrophoretic force. In the final part, water droplets sliding down Fe:$LiNbO_3$ samples are deviated in their motion by hydrophilic paths imprinted by a light stripe, thus demonstrating the validity of the devised OW technique.
This project took place at Laboratorio di Fisica delle Superfici ed Interfacce (LaFSI) and was the result of a joint collaboration with the $LiNbO_3$ Group at the Physics and Astronomy Department of the University of Padova.

The thesis is organized in five chapters, as specified in the following:

Chapter 1

The theoretical concepts of surface wetting are recalled and the description of Liquid-Infused Surfaces (LIS) is given. The characteristic of ElectroWetting (EW) technique is described.

Chapter 2

The main properties of lithium niobate are presented, from the chemical composition, to the crystalline structure and physical and optical features. The photovoltaic effect exploited in this work for droplet manipulation is described in greater detail.

Chapter 3

The procedures used to produce the Fe:$LiNbO_3$ samples and the characterization of their compositional properties by optical absorption measurements are presented. The composition of different hydrophobic coatings to be realised on lithium niobate crystals and the recipes for their production are also reported.

Chapter 4

The optofluidic setup, the instruments used for the acquisition and the protocol for data collection are described.

Chapter 5

The analysis of experimental data is performed and the results are discussed.

Chapter 1

Wetting

This first chapter introduces the wetting phenomena, giving some definitions, such as surface tension, contact angle and hysteresis, fundamental to understand the primary goal of the thesis work, that is the control of sliding micro-droplets. Moreover, an insight into surface functionalization used to favor the slip is presented, expliciting the Liquid-Infused Surface (LIS) method to obtain a hydrophobic and completely flat substrate.

1.1 Interfaces and Surface Tension

An interface is the geometrical surface that separates two systems, like a water drop surrounded by air.
Droplets characterized by small dimensions, such as those used for microfluidic experiments (of the order of μl or nl), are strongly affected by phenomena that occur at these interfaces and that can overwhelm bulk effects, since there is a huge surface/volume ratio.
The discontinuity at the interface between two fluids is a consequence of intermolecular forces between molecules, in particular cohesive forces, like Van der Waals interactions (most generally, London interactions) for organic liquids or hydrogen bonds for water.
Bulk molecules interact with neighbours that surround them in all directions, while molecules sitting at the interface are affected by half neighbours, as shown in Fig. 1.1. For this reason, the former ones experience a total bonding energy U_B per molecule derived by cohesion, while the latter ones gain only $U_S = U_B/2$. In other words, to move a molecule from the bulk to the interface costs an energy of about $U_B/2$. The shape taken by the drop is the result of free energy minimization; therefore, it tends to reduce its surface area and, in the absence of other interactions, the final appearance is perfectly spherical, like a balloon or a soap bubble.
The cost of energy per unit area that opposes a distortion is quantified by the surface tension γ, of the order of $\gamma \approx U_B/(2a^2)$ for a molecule with dimension a and exposed area a^2 [10].
An increase of the drop surface, thinkable as a stretched membrane, can be obtained by an external work:

$$\delta W = \gamma dA$$

proportional to the number of molecules that must be brought up to the surface dA.
The surface tension can also be defined in terms of free energy that contributes to thermodynamic work:

$$\gamma = \left(\frac{\partial F}{\partial A}\right)_{T,V,n}$$

at fixed temperature T, volume V and number of molecules n.

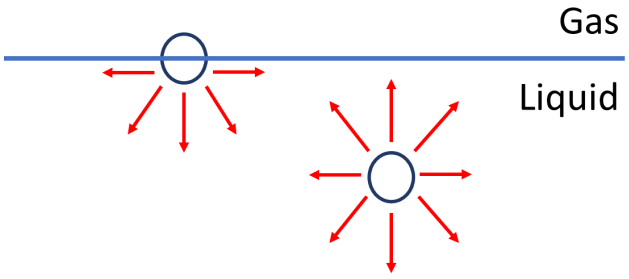

Figure 1.1: Surface and bulk molecules of a fluid.

In S.I. it has unit of J/m^2 (or equivalently N/m) and its value for water in air is $\gamma \approx 72$ mJ/m^2. In the case $\gamma = 0$, the two fluids are said to be miscible.
The surface energy is at the origin of the difference in pressure Δp across the curved surface between two liquids, as described in the Young-Laplace's law:

$$\Delta p = \gamma \left(\frac{1}{R_1} + \frac{1}{R_2} \right)$$

that is inversely proportional to the radii of curvature R_1 and R_2 of the interface.
A useful dimensionless parameter is the Bond number Bo, an index of the strength of gravity with respect to surface tension, defined as:

$$Bo = \frac{\varrho g L^2}{\gamma} = \left(\frac{L}{\lambda_c} \right)^2 \tag{1.1}$$

where ϱ is the liquid density, g is the gravity acceleration, L is the characteristic length of the system. λ_c is the capillary length:

$$\lambda_c = \sqrt{\frac{\gamma}{\varrho g}}$$

that represents the typical dimension below which gravity effect can be neglected. For pure water at 20°C, $\lambda_c \approx 2.7$ mm. For $Bo < 1$ surface tension dominates, while for high values ($Bo \gg 1$) surface effects do not affect the system. Since water droplets having a volume between 1 and 5 μl (thus, a characteristic length of the order of 1-2 mm) are analyzed during the static experiments carried out in this thesis, Bond numbers result to be less than unity and so gravity does not affect the spherical shape of the profile.
For droplets moving with a characteristic velocity v, it is useful to introduce the Capillary number Ca, which quantifies the ratio between shear, viscous forces and capillary forces:

$$Ca = \frac{\mu v}{\gamma}$$

where μ is the dynamic viscosity of the drop. Again, for small Ca numbers, the drop dynamics is dominated by capillary effects.
The correlation between the Bond number and the Capillary number will be investigated in Sec. 5.1, in which surfaces functionalized in different manners are compared.

1.2 Wetting on Surfaces

When liquids are deposited on a plate, they can spread differently according to the nature of the solid surface, the liquid itself and the surrounding gas. The wetting of a surface by a liquid has been studied for two centuries and is found to depend on both the cohesion between molecules in the liquid and the adhesion to the surfaces. The liquid can either spread completely all over the surface and form a film (*total wetting*), or it can form a droplet (*partial wetting*). The two cases can be discriminated by the so-called *spreading parameter* S:

$$S = \gamma_{SV} - \gamma_{LS} - \gamma_{LV}$$

which takes into account the three interfaces, and their respective surface tensions, that characterize the system: liquid-solid γ_{LS}, solid-vapor γ_{SV} and liquid-vapor γ_{LV} tensions. If $S > 0$ the liquid spreads on the solid surface; if $S < 0$ the liquid forms a drop. In the second case, the line where the three phases come together is defined as the *contact line* and it delimits the wetted area.
The tangential angle at the three-phase interface, *i.e.* the *contact angle* θ_Y shown in Fig. 1.2, describes the wettability of the surface with respect to the liquid. It is derived by imposing that the net resultant of the forces on the surface must be zero. In such a way the expression for the Young's equation, derived in 1805 [11], is found:

$$\gamma_{SV} = \gamma_{LV} cos\theta_Y + \gamma_{SL} \tag{1.2}$$

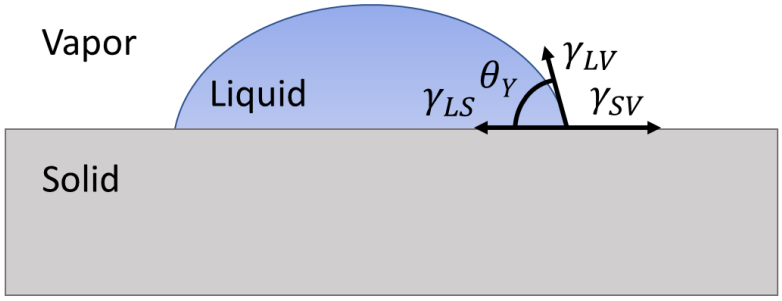

Figure 1.2: Surface tensions of a three-phase interface and contact angle.

The degree of wetting can be divided in different regimes [12], reported in Fig. 1.3, depending on the angle formed over the contact line[1]:

- $\theta_Y < 5°$, superhydrophilic surface;
- $5° < \theta_Y < 90°$, hydrophilic surface;
- $90° < \theta_Y < 150°$, hydrophobic surface;
- $\theta_Y > 150°$, superhydrophobic surface;

[1] In general, for a drop whose liquid is not water you use the prefix *lyo-* instead of *hydro-*.

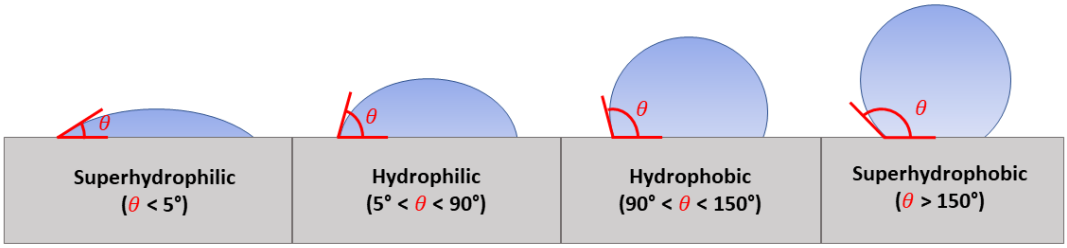

Figure 1.3: Different regimes of wettability for a solid surface.

1.3 Contact Angle Hysteresis

In an ideal situation, the drop at equilibrium forms always the same contact angle θ_Y when deposited on the same surface. In real cases, instead, any surface presents inhomogeneities and defects, so that the static contact angle at the interface is no more θ_Y, as derived from the condition of mechanical equilibrium, but it can assume values in a certain range, maintaining the contact line pinned.
The *contact angle hysteresis* is defined as:

$$\Delta\theta_H = \theta_A - \theta_R$$

where θ_A is the *advancing angle*, that is maximum angle above which the front starts to advance, and θ_R is the *receding angle*, the minimum angle below which the rear starts to recede. The minimum tilting angle of the surface α^* above which the drop starts to move down is called *critical sliding angle*, as displayed in Fig. 1.4. It is intimately correlated with the contact angle hysteresis: the greater $\Delta\theta_H$ is, the more the surface must be inclined to permit the droplet to move.
Another possible method to measure the above-mentioned angles is by inflating and deflating a sessile drop and evaluating the two opposite thresholds at which the contact line starts to move as the drop volume increases or decreases.
A high hysteresis $\Delta\theta_H$ indicates a strong interaction between the liquid and the underlying surface, because of its roughness or chemical defects; on the contrary, low hysteresis means that droplets can move easily over the substrate.

1.4 Lubricant-Impregnated/Liquid-Infused Surface (LIS)

Since the last decade, several studies on surface chemistry and roughness have been carried out, in order to reproduce non-wetting properties useful for commercial and technological applications [13, 3, 4]. These studies were inspired by nature, in which a plethora of plants with self-cleaning [14], slippery [15] or hydro-repellent [16] leaves exists. They can either completely repel water, such as in the case of *lotus*, or trap insects and let them slide inward, like in carnivourus *Nepenthes*.
In 2011, Wong *et al.* produced the first omniphobic *Lubricant-Impregnated Surfaces* (or *Liquid-Infused Surfaces*, *LIS*) by perfusing Teflon nanofibrous membranes with Fluorinert FC70 [17]. They were inspired by *Nepenthes pitcher* plants, whose peristome, composed of microstructures,

can trap a thin layer of water, resulting in a slippery interface in contact with the legs of insects[2]. In order to diminish the contact of the interface with the liquid, surfaces can be functionalized with appropriate micro-/nano-structures that can trap air pockets, exhibiting a non-wetting behaviour [18, 19]. In this case, the contact angle of a drop leaning on the surface is far greater than 90°.
As a matter of fact, since surface is not flat, the drop is affected only by the percentage ϕ_s of solid which is in contact with. Therefore, the apparent contact angle θ^* is different from the ideal one θ_Y and, at equilibrium, is calculated from:

$$\cos\theta^* = -1 + (1 + \phi_s)\cos\theta_Y \tag{1.3}$$

The less the fraction ϕ_s is, the more $\cos\theta^*$ approaches the minimum value -1 and the angle becomes $\theta^* \approx 180°$. The regime is called *Cassie-Baxter state* and in this situation a droplet easily rolls off when the substrate is slightly tilted.
However, these air pockets are not stable because they can collapse by external liquid pressure or disappear when the texture is damaged. The drop placed on the rough surface can then be in complete contact with it, following all the topological deformations of the material. By defining r as the ratio between the total real area and the projected area, the minimization of surface energy yields:

$$\cos\theta^* = r\cos\theta_Y \tag{1.4}$$

that characterizes the *Wenzel state*. Since there exists no surface perfectly flat, r usually is assumed to be (at least slightly) larger than 1.
Eq. 1.4 predicts that roughness enhances wettability: a hydrophilic solid ($\theta_Y < 90°$) becomes even more hydrophilic when it is rough ($\theta^* < \theta_Y$). Conversely, for a hydrophobic solid ($\theta_Y > 90°$) the hydrophobicity is increased ($\theta^* > \theta_Y$) [13].
This regime exhibits a huge hysteresis, so that drops remain pinned because of the strong adhesion between water and the solid surface, as seen in the so-called *rose petal effect* [20].
To reduce pinning or contact angle hysteresis, surfaces with microscopic pockets can be filled with a lubricating liquid, rather than with air, trapped in the texture. Accordingly, a LIS is characterized by a very low contact angle hysteresis, typically below than 5°, and very low drop adhesion.
The lubricant is held on the surface by a microstructured and chemical functionalized substrate that forms small cavities in which capillary forces dominate. The texture must also have a degree of wetting that matches the one of the overlying lubricant in order to be filled completely.
As shown in Fig. 1.4, liquid-infused coatings permit droplets to slip even for small tilting angles. Various configurations for the four-phase system solid-oil-water-air can be analyzed, as reported by Varanasi *et al.* in [19]. When the lubricating oil is added, the so-called *wetting ridges* formed around the base of a droplet on the surface play an important role to the slowing down of the drop moving down the incline.
It is found that the most stable condition, with the lowest interfacial energy, requires the complete impregnation without emergent features (*i.e.* encapsulation).
The sliding critical angle α^* is ideally zero for complete wettability, reached for example with silicone oils; nevertheless, also in case of non-complete encapsulation, very small α^* can be obtained by the fabrication of nanostructures over the pillars.
There exist many different recipes to fabricate LIS and the ones we have used for the experiments of this thesis will be described in details in Sec. 3.5.

[2]This kind of surfaces are also called *Slippery Liquid-Infused Porous Surfaces* (*SLIPS*), because of the porous structure created to trap the impregnating liquid.

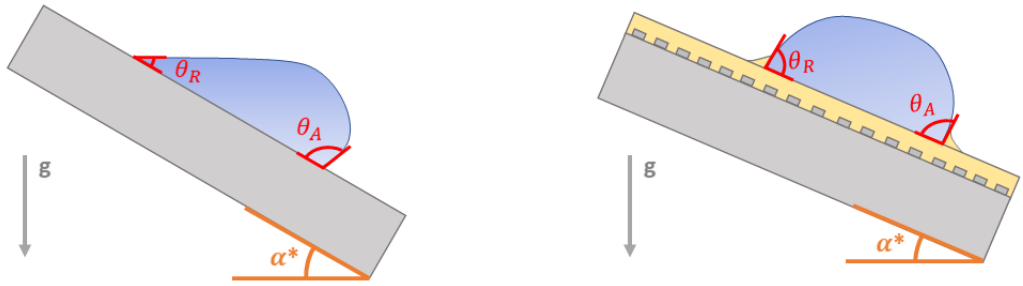

(a) High hysteretic surface

(b) Low hysteretic surface

Figure 1.4: Hysteresis of contact angle on a rough surface (a) and a Liquid-Infused Surface (b). Advancing θ_A and receding θ_R angle are reported in both cases, defined for $\alpha = \alpha^*$ tilting angle. The substrate covered with LIS, forming wetting ridges around the drop, is characterized by low hysteresis.

1.5 Electrowetting

Microfluidic studies have been conducted with the aim of manipulating droplets, controlling their sorting, merging and mixing for chemical or biomedical applications. Droplet manipulation can be achieved by controlling the interfacial energy of the surface over which the liquid has to be moved.

The most used technique in the past two decades based on this principle is the *electrowetting* (*EW*) [21], owing to its ability to electrically direct droplets of small dimensions, its long term reliability and its lack of movable mechanical parts.

The discovery of this phenomenon goes back to the report on the electrocapillarity phenomenon by Lippmann, in 1875 [22]. He found that by applying a voltage between mercury and aqueous electrolytes it is possible to control the position of the mercury meniscus in a capillary.

The first devices used for the purpose of controlling polar liquids were realized by two metallic electrodes in contact with the drop. The application of a voltage difference among the two electrodes promotes the formation of a local concentration of charges in the metallic surface that gives rise to the *electric double layer* at the solid-liquid interface [5]. However, beyond certain voltages (hundreds of millivolts) water undergoes electrolysis at the metallic surface and the system is not stable.

To fix the problem, Berge introduced a thin insulating layer to separate the liquid from the metallic electrode below [23]. This development of the technique takes the name of *electrowetting-on-dielectric* (*EWOD*). In this configuration, schematized in Fig. 1.5, when an electric field is applied across the dielectric layer it tends to pull the droplet down onto the electrode. The polarization charge in the dielectric layer in fact interacts with the dipole molecules in the liquid. This electrostatic interaction causes a decrease in the contact angle, appearing as a change in wettability at the solid-liquid interface.

In the EWOD geometry, the system electrode-dielectric-droplet can be approximated as a series of two capacitors: the metal-dielectric interface and the dielectric-drop interface. The former capacitor has a capacitance $c_d = \epsilon_0\epsilon_d/d$, where ϵ_d is dielectric constant of the insulator and d its thickness; the latter has a capacitance per unit area $c_H = \epsilon_0\epsilon_1/d_H$, where ϵ_1 is the dielectric constant of the liquid and d_H is the thickness of the electric double layer, that is nanometric in most cases. Since the dielectric layer is (most of the times) much greater than the double layer, $d_H \ll d$, the total capacitance is $c \approx c_d$. As a result, the voltage drop occurs within the dielectric

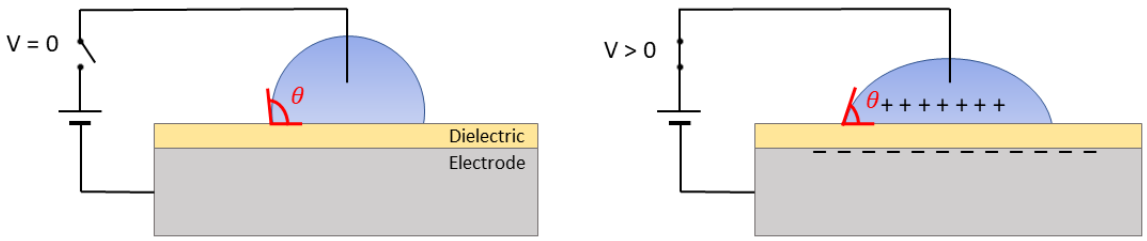

(a) No voltage applied.

(b) Voltage V applied.

Figure 1.5: Electrowetting phenomenon on a surface conveyed by electrodes. If no voltage difference is applied (a), a drop forms an high contact angle θ above the dielectric (and hydrophobic) coating; when an electric field is switched on (b), the contact angle decreases, mirroring an hydrophilic behaviour.

layer. The entire dielectric layer is considered part of one effective solid–liquid interface with a thickness of the order of d [5].
For low voltages, the effective interfacial tension is found to be:

$$\gamma_{SL}^{eff} = \gamma_{SL} - \frac{\epsilon_0 \epsilon_d}{2d} V^2$$

where V is the applied potential difference. Combining with Young expression in Eq. 1.2 for the contact angle, the formula obtained is:

$$\cos\theta = \cos\theta_Y + \frac{\epsilon_0 \epsilon_d}{2d\gamma_{LV}} V^2$$

In order to obtain a conspicuous variation of the contact angle, the initial angle must be very high, hence the dielectric layer should behave as a phobic coating, and its thickness must be as thin as possible.
Beyond a certain threshold voltage, that depends on system components, the contact angle becomes independent on the applied voltage (*contact angle saturation*) and no voltage-induced transition from partial to complete wetting has ever been observed. Even if numerous mechanisms have been proposed to explain these experimental observations, no consistent picture of contact angle saturation has emerged.
Activating droplets in EWOD is affected by pronounced oscillations in response to an abrupt external stimulus, resulting in elongated times to reach the equilibrium state, mediated by the contact line frictional force [24].
Thus, a new electrowetting approach is the *electrowetting on liquid-infused film* (*EWOLF*) that features a liquid-infused film as the dielectric layer to impart complete reversibility and droplet oscillation suppression during the transient response [6]. Instead of using chemically hydrophobic insulator made of polymeric materials, the hydrophilic surfaces are usually covered by fluorinated silanes or amorphous fluoropolymer coatings, like polytetrafluoroethylene (PTFE), in which lubricating oil infiltrates. However, these techniques requires precautions on the electrode manifacturing and the voltage applicable.

This work will present an alternative method to control droplets, that exploits a particular substrate, the lithium niobate, whose faces can be charged when exposed to light. These photoinduced surface charges can mimic the effect of an electric field provided by electrodes in a manner better explained in the following chapter.

Chapter 2

Lithium Niobate

In this second chapter, the chemical composition and the crystallographic structure of lithium niobate are reported, together with its chemical and physical properties. This material is used as a substrate because of its photovoltaic effect, exploited for the purpose of driving water droplets by means of light.

2.1 Chemical Composition

Lithium niobate ($LiNbO_3$, written also as *LN*) is a solid, synthetic material, non present in nature, that is derived from the pseudo-binary system Li_2O-Nb_2O_5. It is colourless, insoluble in water and in organic solvents and has a high melting point (about 1260°C). It is characterized by several optical and mechano-physical properties, such as electro-optical and non-linear optical coefficients, high piezoelectricity and pyroelectricity, photovoltaic and photorefractive behaviour, that are well-known in photonics and integrated optics and that will be described exhaustively in Sec. 2.3.

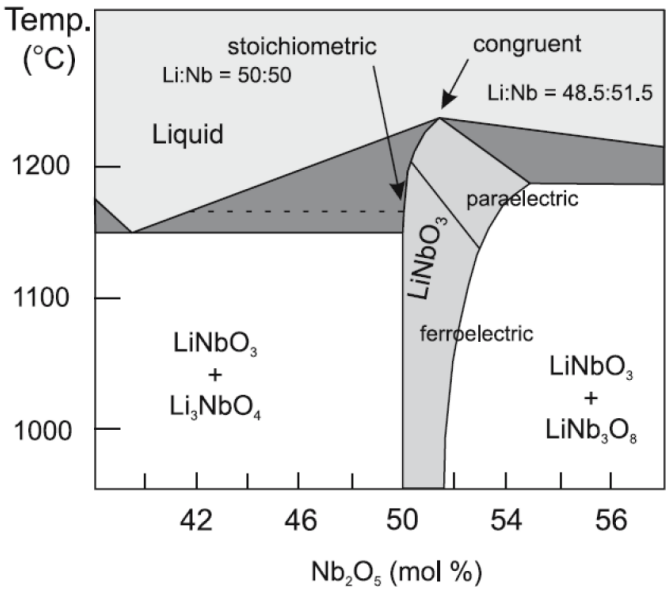

Figure 2.1: Phase diagram of Li_2O-Nb_2O_5 system [9].

By varying the percentage of the two oxides in the pseudo-binary system, a phase diagram for different temperatures can be built as reported in Fig. 2.1. It shows that, among all possible compounds, the maximum of the solid-liquid curve corresponds to the *congruent* composition of the crystal, characterized by lithium deficiency (48.5%). In this case, the melted and the solid constituents used during the growth have the same composition, allowing the formation of a uniform final product, by means of the Czochralski technique[1].
In the *stoichiometric* composition, instead, both Li_2O and Nb_2O_5 are present with percentage of 50%, but the melt and the crystal can slightly vary during the growth, thus resulting in a non-uniform sample, particularly along the growth axis. The percentages of the two oxides determine the ratio between concentration of Li and Nb, that affects several properties of $LiNbO_3$ like phase transition temperature, birefringence, photovoltaic effect, and UV absorption edge. For their uniform composition and high stability achieved during the growth process, congruent wafers are preferred for commercial production and practical applications.

2.2 Crystal Structure

The crystallographic structure of lithium niobate can be described by choosing among three different cells, that can constitute the whole system: hexagonal, rhombohedral or orthohexagonal. The preferred choice for most applications is the orthohexagonal (Fig. 2.2), even if also the former two are convenient for certain structural investigations.
At room temperature the crystal exhibits a mirror symmetry about three planes that are 60° apart. The axis obtained by their intersection is the center for a three-fold rotational symmetry of the crystal. The orthohexagonal convention provides that the three mutually orthogonal reference axes are:

- $\hat{z}$-axis (identified with the $\hat{c}$-axis, or optical axis) around which the crystal exhibits its three-fold rotation symmetry;
- $\hat{y}$-axis, laying on one mirror plane;
- $\hat{x}$-axis, perpendicular to both previous axes.

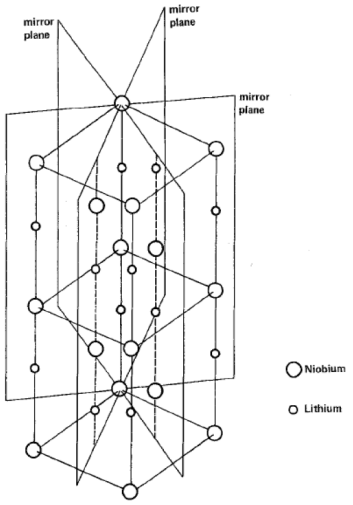

Figure 2.2: Orthohexagonal crystallographic structure [25].

[1]For a description of the technique, see Sec. 3.1

Both $\hat{z}$-axis and $\hat{y}$-axis are interested by piezoelectricity and, by convention, their positive direction is chosen to be pointing on the surface that becomes negatively charged under uniaxial compression. The $\hat{z}$-axis is also pyroelectric and the positive direction is the one towards the plane positively charged by cooling the crystal.
Below a critical temperature, called Curie temperature T_C (of about 1140°C for *congruent* composition), lithium niobate is a ferroelectric material, *i.e.* it has a spontaneous polarization, that can be reversed by applying high electric fields. Above T_C instead, the spontaneous polarization disappears and the crystal is subjected to the paraelectric phase. In this regime, the crystal consists of planar sheets of oxygen atoms along $\hat{c}$-axis, arranged in triangular configurations rotated by approximately 180°. Li ions are located in the center of the oxygen triangles, while Nb ions are located at the center of an octahedron formed by two triangles (Fig. 2.3a).
Instead, in the ferroelectric phase, the structure exhibits a slightly distorted hexagonal close-packed configuration, in which ions move along $\hat{c}$-axis, giving rise to a net dipolar moment. The octahedral interstices formed in between oxygen planes are one-third filled by lithium atoms, one-third by niobium and one third is vacant (Fig. 2.3b).
Moreover, in *congruent* composition, some Nb ions can occupy the lattice site of Li, remained empty because of the lower percentage of Li in the material, if compared to the stoichiometric 50%-50% composition: these atoms are called Nb antisites (Nb_{Li}) [25].

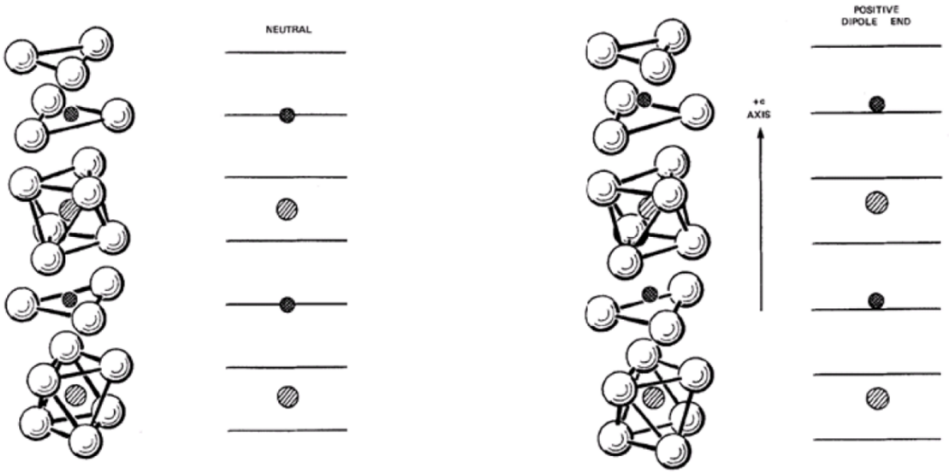

(a) Paraelectric phase **(b)** Ferroelectric phase

Figure 2.3: Li, Nb and vacancies disposition along $\hat{c}$-axis of $LiNbO_3$ in paraelectric (a) and ferroelectric (b) phase [25]. O ions are depicted with white big circles; single cross-hatched circles corresponds to Nb ions, smaller and darker circles to Li ions.

2.3 Physical Properties

In this section, the most significant properties of lithium niobate, from optical effects (like birefringence and electro-optic effect, photorefractive effect) to phenomena able to induce polarizations (such as piezo-/pyro-electricity) are listed. A detailed description of the photovoltaic effect, exploited during this work, will be instead reported in Sec. 2.4.

2.3.1 Refractive Indices: Birefringence and Electro-Optic Effect

A generic anisotropic material responds to an electrical stimulus in a proportional manner to the external electric field, depending upon the direction of the **E** field considered. The magnitude of this response is provided by the dielectric permettivity tensor $\hat{\epsilon}$, so that the linear relation between the displacement vector **D** and the electric field **E** can be written as $\mathbf{D} = \hat{\epsilon}\mathbf{E}$.
For lithium niobate, considering the orthohexagonal system, the permettivity second-rank tensor can be represented by a 3×3 matrix:

$$\hat{\epsilon} = \begin{pmatrix} \epsilon_{11} & 0 & 0 \\ 0 & \epsilon_{11} & 0 \\ 0 & 0 & \epsilon_{33} \end{pmatrix}$$

Permettivity components are found from experiments on low-frequency capacitances of two thin flat-plate specimens and their values at acoustic frequencies, normalized in terms of permettivity of vacuum ϵ_0, are $\epsilon_{11}/\epsilon_0 = 84.1$ and $\epsilon_{33}/\epsilon_0 = 28.1$ [25].
It is worthy to note that the matrix is diagonal and the components related to directions perpendicular to the $\hat{c}$-axis are equal. At optical frequencies, the permettivity is described in terms of the refractive index, intimately correlated to optical properties. There exist two different refractive indices: the ordinary (n_o) index, referring to $\hat{x}$ and $\hat{y}$ direction, and the extraordinary (n_e) index, referring to the $\hat{z}$ direction. Their relation with the components of $\hat{\epsilon}$ tensor are:

$$n_o = \sqrt{\frac{\epsilon_{11}}{\epsilon_0}} \quad n_e = \sqrt{\frac{\epsilon_{33}}{\epsilon_0}}$$

For congruent crystals, the ordinary and extraordinary refractive index measured at wavelength of 530.0 nm with Nd laser at 24.5°C are respectively $n_o = 2.3247$ and $n_e = 2.2355$ [25].
These two different n_o and n_e give rise to the birefringence experienced by an incident radiation whose polarization has a component parallel to the optical axis $\hat{c}$. The dispersion law is found to depend also on the temperature and on the concentration of lithium in the material, accordingly to the formula proposed by Schlarb and Betzeler [26].

As a second-order optical phenomenon, the electro-optic effect consists in a change of the refractive index upon the application of an electric field. This variation can be expressed as a function of the electric field **E**, as a series of powers, truncated at the second order:

$$\Delta\left(\frac{1}{n^2}\right)_{ij} = \sum_k r_{ijk}E_k + \sum_{ijkl} s_{ijkl}E_kE_l$$

where the third-rank tensor r_{ijk} and the fourth-rank tensor s_{ijkl} refer to the linear and quadratic electro-optic effect, usually named *Pockels effect* and *Kerr effect* respectively. In lithium niobate, the Kerr effect can be neglected since the quadratic electro-optic effect has been observed to be significant only above 65 kV/mm of applied field [27]; hence, in most cases the dependence of refractive index variation upon **E** is linear.

It depends moreover on the incident light polarization. For a light beam polarized along the optical axis and propagating either along $\hat{x}$ or $\hat{y}$ directions, the variation of the ordinary and extraordinary refractive indices are derived from the following relations:

$$\Delta n_o = -\frac{1}{2} n_0^3 r_{13} E_z \quad \Delta n_e = -\frac{1}{2} n_e^3 r_{33} E_z$$

while, in the case of polarization either along $\hat{x}$ or $\hat{y}$-axis and propagation along $\hat{z}$ direction:

$$\Delta n_o = -\frac{1}{2} n_0^3 r_{22} E_x \quad \Delta n_e = 0$$

The electro-optic linear coefficients in the previous formulas belong to a reduced r tensor, whose definition and values are given by Bernal *et al.* [28].

2.3.2 Piezoelectric and Pyroelectric Effects

Lithium niobate is also a piezoelectric material, *i.e.* it is possible to induce on it a certain polarization by applying a mechanical stress and, conversely, can exhibit an elastic strain under the application of a voltage. The relation between the polarization induced along i-direction and the second-rank stress tensor σ_{jk} is linear, given by:

$$P_i = \sum_{jk} d_{ijk} \sigma_{jk}$$

where d_{ijk} is the third-rank piezoelectric tensor.

Furthermore, it shows a pyroelectric behaviour, *i.e.* it exhibits a change in the spontaneous polarization as a function of temperature. Again the relation between the change in temperature (ΔT) and in the spontaneous polarization (ΔP) is linear, writable as $\Delta P = \hat{p} \Delta T$, where $\hat{p}$ is the pyroelectric tensor. The pyroelectric field obtained from the charge redistribution, performed by the Li and Nb atoms with respect to the oxygen planes, is:

$$\mathbf{E_{pyro}} = -\frac{1}{\epsilon \epsilon_0} \frac{\partial P_s}{\partial T} \Delta T \cdot \mathbf{k_s} \tag{2.1}$$

with a direct proportionality to the change in temperature. The minus sign indicates an antiparallel orientation with respect to the spontaneous polarization direction[2] $\mathbf{k_s}$. This field can likewise be generated by irradiating the crystal, inducing a change in the spontaneous polarization P_s with a local heating of the material.
The pyroelectric effect has been already used to manipulate micro- and nano-droplets by electrophoresis and trap neutral particles via dielectrophoresis [29, 30]. These results further confirm that lithium niobate is a good candidate as a substrate for applications in the field of microfluidics.

2.3.3 Photorefractive Effect

The electro-optic effect, together with the photovoltaic effect, contributes to the interesting phenomenon known as *photorefractive effect*, which consists in the modification of the refractive index of the material by light exposure [9].
This effect relies on the presence of intrinsic and extrinsic impurities with two valence states. In fact they add intermediate levels in-between the valence and conduction bands of the pure

[2] The pedix s stands for spontaneous.

lithium niobate, acting both as donors or acceptors of free charges depending on their valence state. The illumination of the material with light of proper wavelength causes the promotion of electrons from the donor level to the conduction band. By diffusion, photovoltaic effect or drift phenomena the electrons are transferred inside the material till they are trapped by acceptors. If the trapping occurs in a dark region, the electrons can no longer be photoexcited.
As a consequence, an internal space-charge electric field $\mathbf{E}_{sc}$ builds up and modulates the refractive index of the crystal by the above-mentioned electro-optic effect, as shown in Fig. 2.4.

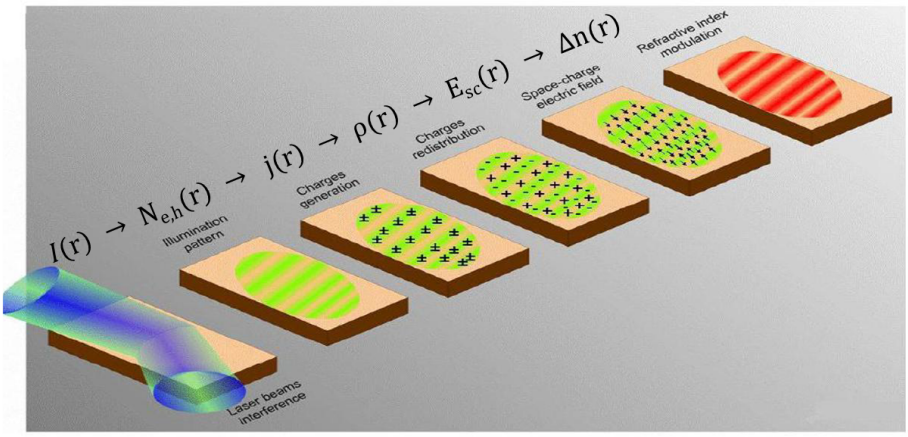

Figure 2.4: Photorefractive effect on lithium niobate.

Intrinsic niobium antisites are present in *congruent* lithium niobate with the two oxidative states Nb_{Li}^{4+} and Nb_{Li}^{5+}, acting as donors and acceptors for the charge carriers: the pentavalent ions trap electrons, transforming themselves into tetravalent ions, that can lose one electron through photoexcitation and return to be Nb^{5+} ions. The space-charge field produced by these ions can reach order of magnitudes of $10^4 - 10^5$ V/m. In order to enhance the effect, crystal are doped with transitium metals, such as iron or copper, able to increase the field up to 10^6 V/m. The most used element is iron, appearing as Fe^{2+} (donor) and Fe^{3+} (acceptor) in a similar way to Nb ions. Other elements, like manganese, are on the contrary used to dope $LiNbO_3$ samples to reduce the photo-voltaic/refractive effect.

2.4 Photovoltaic Effect in Fe:LiNbO$_3$

Lithium niobate crystals exposed to light are subjected to a displacement of the free charges, leading to the rise of a stationary current. This phenomenon is known as bulk *photovoltaic* (or *photogalvanic*) *effect*, discovered in 1964 by Glass *et al.* [8]. The resultant current is proportional to the intensity of light and to the absorption coefficient α of the material, that depends on the wavelength. This effect is highly asymmetric due to the crystallographic structure of the material, with a preferred direction along which the photoexcited charge carriers can move, that is the optical axis $\hat{c}$.
The photovoltaic effect represents an important contribution to the modulation of the refractive index of lithium niobate. Together with a drift component $\mathbf{j}_{drift}$ due to the presence of external electric fields and a diffusion current $\mathbf{j}_{diff}$, the photovoltaic current $\mathbf{j}_{ph}$ can contribute to the movement of charge carriers across the material when this latter is illuminated. Thus, the total

current can be written as:

$$\mathbf{j}_{tot}(\mathbf{r},t) = \mathbf{j}_{drift} + \mathbf{j}_{ph} + \mathbf{j}_{diff}$$

and, in general, it is a function of both space and time.
By defining $\rho(\mathbf{r},t)$ the internal charge density, Poisson equation and continuity equation must hold:

$$\boldsymbol{\nabla} \cdot (\hat{\epsilon}\mathbf{E}) = \frac{\rho}{\epsilon_0}$$

$$\boldsymbol{\nabla} \cdot \mathbf{j} + \frac{\partial \rho}{\partial t} = 0 \tag{2.2}$$

where $\hat{\epsilon}$ is the dielectric tensor of the material (described in Subsec. 2.3.1), ϵ_0 the dielectric permittivity in vacuum and $\mathbf{E}$ the local electric field.

2.4.1 Current Density: Drift, Photovoltaic and Diffusion Contributions

The drift component $\mathbf{j}_{drift}$ arises from the Coulomb interaction between free charge carriers, *i.e.* the electrons in the conduction band and the holes in the valence band, and the electric field and obeys Ohm's law:

$$\mathbf{j}_{drift} = \hat{\sigma}\mathbf{E}, \qquad \hat{\sigma} = q\hat{\mu}_{e,h}N_{e,h} \tag{2.3}$$

where $\hat{\sigma}$ is the conductivity tensor, q the elementary charge, $\hat{\mu}_{e,h}$ the mobility tensor and $N_{e,h}$ the charge carriers density. The total electric field $\mathbf{E}$ consists of three contributions: the space charge field $\mathbf{E}_{sc}$ arising from the light-induced charge redistribution, the external field $\mathbf{E}_0$ and the pyroelectric $\mathbf{E}_{pyro}$, already explained in Eq. 2.1. The latter can also derive from the photo-induced heating of the material, but it is completely negligible in Fe:$LiNbO_3$ for light intensities lower than 10^5 W/m^2.

The photovoltaic current density $\mathbf{j}_{ph}$ is a consequence of the asymmetric energy bands typical of non-centrosymmetric crystals, by which the momentum of photo-excited electrons has a preferential direction. For lithium niobate, this direction corresponds to $\hat{z}$-axis (the crystallographic $\hat{c}$-axis), while along $\hat{x}$ and $\hat{y}$-axis current densities are an order of magnitude lower. The tensor relationship between the short-circuit current density and the illumination can be written as:

$$j_{ph,i} = \beta_{ijk} e_j e_k^*, \qquad i,j,k = 1,2,3$$

where the complex quantity $\beta_{ijk} = \beta_{ijk}^*$ represents the third-rank photovoltaic tensor and e_j and e_k^* are the components of the light complex electric field vector.
A linearly polarized wave is described only by the real part of β_{ijk}, while a circularly polarized wave has also an imaginary part. The photovoltaic tensor has four independent non-zero components: β_{333}, $\beta_{311} = \beta_{322}$, $\beta_{222} = -\beta_{112} = -\beta_{121} = -\beta_{211}$, $\beta_{113} = \beta_{131}^* = \beta_{232}$.
The photovoltaic current density depends linearly on light intensity:

$$j_{ph} = \alpha k_G I = \alpha \frac{\mu \tau_{ph} E_{ph}}{h\nu} I$$

where μ is the mobility of charge carriers, τ_{ph} is the time within which charge carriers contribute to the transport of photovoltaic charge, $h\nu$ is the energy of the incident photons and E_{ph} is a phenomenological introduced field acting on charge carriers.
These quantities determine the so-called Glass constant k_G, which describes the anisotropy of the charge transport and for Fe:$LiNbO_3$ is equal to $2.8 \cdot 10^{-11}$ m/V.

The absorption coefficient α depends on the donor ions concentration [Fe^{2+}] and their absorption cross-section $s_{Fe^{2+}}$:

$$\alpha = s_{Fe^{2+}}[Fe^{2+}]$$

Thus, the photovoltaic current is directly proportional to the amount of Fe donors in the material.

The last contribution to the total current density, the diffusion component $\mathbf{j}_{diff}$, is significant when a charge concentration gradient exists inside the material and is described by the relation:

$$\mathbf{j}_{diff} = -q\hat{D}\nabla N_{e,h}$$

where $\hat{D} = \frac{\hat{\mu}_{e,h}k_BT}{q}$ is the diffusion tensor, q the elementary charge and k_B the Boltzmann constant. Usually for non-uniform illumination with a period larger than 1 μm this contribution is negligible [31].

2.4.2 Charge Transport: One-Center Model

As just mentioned, iron is the most common element used to dope lithium niobate samples. This kind of impurity is observed to be present in two different oxidative states, Fe^{2+} and Fe^{3+}, that act in the crystal as donors and traps, respectively, of free charges, whose generation and recombination is mediated by light.
The mechanism that regulates the transport of the photoexcited electrons[3] is fully explained by a complete set of equations derived by Vinetskii and Kukhtarev [32], valid for light intensities lower than 10^6 W/m^2. The model suggests that only one kind of ions affects the photovoltaic effect (*one-center model*): in this case, the dominant contribution arises from Fe dopants.
The rate of change for the carrier densities N_e (the electron concentration in the conduction band) and for the concentrations $N_{Fe^{2+}}$ and $N_{Fe^{3+}}$ of filled and empty centers are expressed by the following relations:

$$\frac{\partial N_e}{\partial t} = (sI + \beta_T)N_e - \gamma_e N_e N_{Fe^{3+}} - \frac{\boldsymbol{\nabla}\cdot\mathbf{j_{tot}}}{q}$$

$$\frac{\partial N_{Fe^{2+}}}{\partial t} = -\frac{\partial N_{Fe^{3+}}}{\partial t} = -(sI + \beta_T)N_{Fe^{2+}} + \gamma_e N_e N_{Fe^{3+}} \tag{2.4}$$

where s the absorption cross-section, γ_e the recombination constant, μ_e the charge mobility, D the diffusion coefficient, β_T the thermal generation rate.
Taking into account all the significant contributions from $\mathbf{E}$ field, that are the space-charge field $\mathbf{E_{sc}}$ and the external field $\mathbf{E_{ext}}$, the total current is written as:

$$\mathbf{j_{tot}} = q\mu_e N_e \mathbf{E} - qD\nabla N_e + sN_{Fe^{2+}}k_G I\hat{i}$$

where q is the elemental charge and $\hat{i}$ is the versor of the photovoltaic current. The pyroelectric field component is neglected since the intensity reached for the experiment is at most of the order of 10^4 W/m^2.
For space-charge field, also the Poisson equation:

$$\boldsymbol{\nabla}\cdot(\hat{\epsilon}\epsilon_0\mathbf{E_{sc}}) = \rho = q(N_e + N_{Fe^{2+}} - N_{Fe^{2+}}(0)) \tag{2.5}$$

must hold, with $N_{Fe^{2+}}(0)$ the initial donor concentration before light excitation.

[3] In Fe:LiNbO$_3$ samples for illumination in the visible range only electrons contribute to charge transport phenomena [31].

Since $N_e \ll N_{Fe^{2+}}$, its contribution in Eq. 2.5 can be neglected. However, in the term $\partial\rho/\partial t$ of Eq. 2.2 there is also a contribution from the temporal derivative of N_e, a priori non negligible. After having switched-on the light source, a stationary state is reached almost instantaneously and N_e remains constant, being at any time in quasi-equilibrium with the traps distribution. The initial transient time for N_e in $LiNbO_3$ is in the ps scale and if the light pulse duration is longer than this time interval, in which the space-charge field built-up is not appreciable, the *adiabatic approximation* is valid. This holds also for $N_{Fe^{2+}}$, thus from Eq. 2.4:

$$N_e(\mathbf{r},t) = \frac{(sI(\mathbf{r}+\beta_T))}{\gamma}\frac{N_{Fe^{2+}}(\mathbf{r},t)}{N_{Fe^{3+}}(\mathbf{r},t)}$$

By sostituting into Eq. 2.3, the conductivity is equal to:

$$\sigma = e\mu\frac{s}{\gamma}\frac{N_{Fe^{2+}}}{N_{Fe^{2+}}}I + e\mu\frac{\beta_T}{\gamma}\frac{N_{Fe^{2+}}}{N_{Fe^{3+}}} = \sigma_{ph} + \sigma_{dark} \tag{2.6}$$

The photoconductivity results to be the sum of a term σ_{ph} proportional to the light intensity I and a contribution σ_{dark} (dark conductivity) due to the thermal excitation of the charge carriers in absence of external radiations. However, for intensities of the order of 10^4 W/m^2, the excitation derived from illumination prevails on thermal effects at room temperature and σ_{dark} component becomes negligible [33]. On the contrary, in absence of light the σ_{dark} component dominates, which induces the erase of the previously light-induced charge separation.
Both conductivities depend on the *reduction degree*:

$$R = \frac{N_{Fe^{2+}}}{N_{Fe^{3+}}} = \frac{[Fe^{2+}]}{[Fe^{3+}]} \tag{2.7}$$

i.e. the ratio between the concentrations of donors and acceptors. Therefore, it is evident that increasing the number of donors would enlarge both R and σ.

2.4.3 Space-Charge Field

In order to write patterns on the lithium niobate samples, contributions from Fe doping must be well taken into considerations. It has been seen that light illumination generates an electric field along the preferred $\hat{z}$-axis that establishes a refractive index variation via electro-optic effect.
The internal space-charge field $\mathbf{E_{sc}}$, a consequence of the charge redistribution along $\hat{c}$-axis, arises with an exponential dependence on time spent for lighting up the crystal:

$$\mathbf{E_{sc}} = -\mathbf{E_{ph}}(1 - e^{-t/\tau}) \tag{2.8}$$

where τ is the characteristic time of the process and $\mathbf{E_{ph}}$ is the photovoltaic field, defined as:

$$\tau = \frac{\epsilon_{33}\epsilon_0}{\sigma_{ph}} = \frac{\epsilon_{33}\epsilon_0\gamma}{e\mu sI}\frac{[Fe^{3+}]}{[Fe^{2+}]} \quad \text{and} \quad E_{ph} = \frac{k_G\gamma}{e\mu}[Fe^{3+}] \tag{2.9}$$

This field $\mathbf{E_{ph}}$ represents the maximum possible space-charge field, reached ideally at infinite time (asymptotic value), and it is proportional only to the Fe oxidation state related to trap concentration.
From the definition of the photoconductivity σ_{ph} in Eq. 2.6, the characteristic time τ is inversely proportional to the reduction degree of the material.
Taking this into account, a convenient way to speed up the process is to increase the reduction degree of the material by reducing the $LiNbO_3$ sample, *i.e.* increase the amount of donors. However, this goes to the expense of the space-charge field, directly dependent on $[Fe^{3+}]$, and so of the final amount of charges in the two distributions that forms at the opposite side with respect to $\hat{z}$-axis.

2.5 Optowetting on Lithium Niobate with LIS Coating

Since the goal of this thesis is to manipulate droplets, the novel idea is to exploit the photovoltaic effect, proper of lithium niobate, to tune the wettability of the surface of the material. The standard electrowetting technique, already described in the Sec. 1.5, requires the fabrication of specific electrodes for any geometry to be considered. The use of $LiNbO_3$ instead would permit to overcome this limitation by creating charges directly on the surface, through the photovoltaic current, producing paths on the sample that can be erased and rewritten simply with a light source properly spatially modulated. The easy reconfigurability of such approach represents also the main advantage with respect to other methods, such as the pyroelectric effect reported in [29, 30], where fixed and time consuming periodically poled structures are created or expensive instrumentations are required. We call this new function *optowetting* (*OW*).
On a z-cut $LiNbO_3$ crystal[4] illumination causes the excitation of free carriers, their separation along the $\hat{z}$-axis and so the formation of charged regions on the two main faces of the substrate. In particular, there will be the establishment of a local negative charge concentration on the +z side of the sample and a positive one on the opposite face (Fig. 2.5a).
On x-cut (or y-cut) samples with the main face perpendicular to the $\hat{x}$-axis (or $\hat{y}$-axis), conversely, the $\hat{z}$-axis lies on the surface, so the distribution of charges is splitted in two specularly opposed side in each face, that is the charge accumulates at the borders of the illuminated spot (Fig. 2.5b).
Since in iron-doped lithium niobate crystals (Fe:$LiNbO_3$) the photovoltaic effect is increased at least by one order of magnitude with respect to the undoped material, they are preferable for the purpose of manipulating droplets. Therefore, this typology of samples is utilized to perform systematic measurements of optowetting and to continue the study of dynamic behaviour of droplet on tilted samples covered with LIS, as investigated in previous thesis works [34, 35].

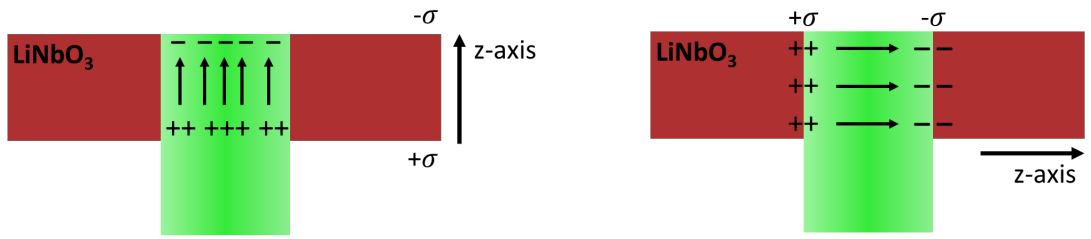

(a) z-cut sample

(b) x-cut (or y-cut) sample

Figure 2.5: Photovoltaic effect on Lithium Niobate sample.

[4]The name z-cut refers to the kind of cut, parallel to the optical $\hat{c}$-axis, as explained better in Sec. 3.2.

Chapter 3

Fe:$LiNbO_3$ Sample Production

In this chapter the method used to grow, cut and polish the samples employed during this work is explained. Optical absorption measurements performed to get crystal properties after doping are presented. Finally, different type of surface functionalizations used to realize hydrophobic coatings on the crystals are described.

3.1 Sample Growth: Czochralski Technique

As already mentioned in the previous chapter, in order to improve the effect of photorefractivity, a lithium niobate crystal can be doped with transition elements, like iron. This expedient permits to increase the photovoltaic current by an order of magnitude with respect to the pure crystal thus making more efficient the light-induced manipulation.
One possible way to dope the lithium niobate matrix with Fe ions is represented by the Czochralski technique [36], thus named after the polish Jan Czochralski who invented it in 1915, and it is usually referred as *bulk* doping. This method, utilized to obtain single crystals of metals and more often of semiconductors (*e.g.* silicon wafers), consists on the controlled solidification of a melt around a prototype germ of the desired material.
The lithium niobate seed is placed on a rod-shaped aluminum carrier and put into a tubular furnace. This latter is heated to reach a temperature above the melting one (1260°C) and contains a platinum crucible with the doped melt that has to be crystallized. Once the contact between the see and the molten material has been realised, into the molten material, the seed rod is pulled upwards and rotated with constant speed to induce a homogeneous solidification of the melt which is grown with the same crystallographic structure of the upper seed. While the rod is raised, the temperature is kept controlled to let the germ increase gradually in diameter from the initial dimension (the *neck*) to the final one (at the *shoulder*). For the rest of the *body*, the diameter is kept constant to form the bottle-shaped *boule*, with a concentration of Fe ions that is the same over the entire crystal.
In-diffused samples are instead obtained by thermal diffusion of an iron thin film, which has been previously deposited on the surface of the lithium niobate substrate via sputtering technique. In this way commercially lithium niobate crystals are locally doped at the surface with a dopant concentration profile that depends on the depth as a semi-gaussian distribution, whose centroid coincides with the surface. By varying the thickness of the iron thin film and the annealing parameters it is possible to tune the higher value of dopant concentration at the surface and its mean depth, which is usually in the range of 1-30 microns. The bulk-doped samples, however, are more convenient since a greater amount of dopants is injected in the whole volume of the

crystal and therefore a higher number of free charges can accumulate at the surface.
Some of the bulk or locally iron-doped (Fe:$LiNbO_3$) samples were prepared by the $LiNbO_3$ group at Physics and Astronomy Department of the University of Padova. The bulk Fe:$LiNbO_3$ sample for final tests of sliding droplets on LIS was produced by Crystal Technology (in Palo Alto, California).

3.2 Sample Preparation: Cutting, Lapping and Polishing

From the grown boule, z-cut samples are prepared by cutting the boule perpendicularly to its longitudinal axis, thus obtaining disc-shaped substrates. During this process, the crystallographic orientation of the main faces of the subsamples is monitored by means of High-Resolution X-Rays Diffraction measurements.
Samples already cut are cleaned with acetone, eventually under sonification with the ultrasonic cleaner (for 10 minutes), and isopropanol.
Finally, crystals are subjected to other two processes in order to obtain surfaces with optical quality: *lapping* and *polishing*. The Logitech PM5 lapping machine is used to perform both treatments by using a rotating iron or polyurethane disc and a *jig*, a device that can hold the crystal and regulate the force applied on the samples, pressed on the disc. A micrometer scale, with a pitch of 1 μm, permits to control the mechanical abrasion rate and consequently the sizes of the possible defects which can be created during the process.
During the lapping procedure, a mechanical arm maintains the jig fixed above the rotating iron disc, over which an abrasive solution containing alumina particles with dimension of about 9 μm lies: this first step reduces the material of about 100 μm, with an upper limit to the erosion rate of 10 μm/min. Defects introduced during this phase do not exceed three times the size of the alumina particles. In the next step, the solution contains particles with a smaller diameter (3 μm) to remove defects previously created, eroding further 40 μm of thickness.
The last polishing process involves the use of a polyurethane disc covered by a colloidal suspension of particles with diameter of 0.1 μm, rotating under the mobile jig. At least 10 μm are abraded and crystal surface optically transparent are obtained.

3.3 Sample Characterization: Optical Absorption

As explained in the previous chapter, the "reduction degree" of Fe:$LiNbO_3$ crystals (*i.e.* the ratio between the concentrations of Fe^{2+} and Fe^{3+}) strongly affects the photovoltaic response of the material. It is then fundamental to determine the amount of these ions in each sample. To this aim, optical absorption measurements were performed on each substrate.
Pure lithium niobate is transparent for a range of wavelengths that goes from 320 nm to 5000 nm for congruent composition [25], having a gap between valence and conduction band of about 4 eV.
The addition of Fe ions creates new absorption bands that interposes the native ones. In fact, after doping, iron is present in two different oxidation states Fe^{2+} and Fe^{3+}, that serve respectively as donors and acceptors of electrons, acting as photo-refractive centers and traps. Their concentration can be modified by treating the sample in a reductive atmosphere (with Ar+H_2 or N_2+H_2, H_2-rich) or oxidizing atmosphere (O_2), to create *reduced* (high [Fe^{2+}]) or *oxidized* (high [Fe^{3+}]) samples.

The optical transitions between middle bands shown in Fig. 3.1 can be explained by the crystal-field theory, that suggests the existence of four principal transitions:

- *A band* at 1.1 eV (1128 nm), transition of only Fe^{2+};
- two *F bands* at 2.57 and 2.91 eV (483 and 426 nm), spin-forbidden transitions of Fe^{3+};
- *D band* at 2.6 eV (477 nm), transition between Fe^{2+} and Nb^{5+} ions, with consequent creation of electrons in the conduction band by Nb^{5+} ions;
- *C band* at 3.1 eV (400 nm), transition between oxygen π-orbitals and Fe^{3+} ions, with consequent creation of holes in the valence band by O^{2-} ion.

Since A and D bands are related only to Fe^{2+}, they can give a quantitative estimation of donor concentration. The concentration of traps $[Fe^{3+}]$ is given by subtracting $[Fe^{2+}]$ from the total concentration of Fe ions known from the doping process.

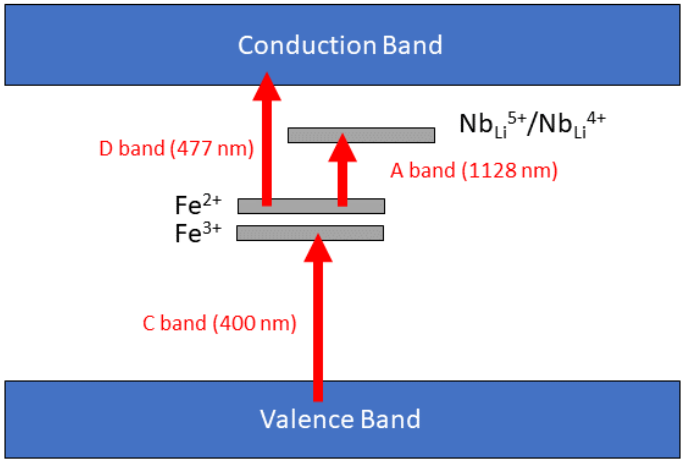

Figure 3.1: Fe-doped Lithium Niobate band scheme.

To evaluate the optical absorption of the crystals a V-670 spectrophotometer is used. It permits to investigate the spectrum in a range of wavelengths from the near-UV (by deuterium lamp, minimum of 190 nm) to the infrared region (by halogen lamp, maximum of 2700 nm).
The illumination provided by the lamp passes through the lithium niobate crystal and the intensity transmitted is lower than the initial one I_0, accordingly with the Lambert-Beer law:

$$I_T(\lambda) = I_0 \gamma e^{-\alpha(\lambda)d} \tag{3.1}$$

where d is the thickness of the sample and α its absorption coefficient for a given wavelength λ. A parameter γ is added to the formula to take into account the reflections on the surfaces.
The spectrophotometer is able to detect the transmittance for a radiation, defined as the ratio between the transmitted intensity and the incident intensity:

$$T(\lambda) = \frac{I_T(\lambda)}{I_0} = \gamma e^{-\alpha(\lambda)d}$$

The transmittance T_s of Fe:$LiNbO_3$ is normalized with the transmittance T_p relative to a pure crystal in the same experimental condition:

$$\frac{T_p}{T_s} = \frac{\gamma_p}{\gamma_s} \frac{e^{-\alpha_p(\lambda)d_p}}{e^{-\alpha_s(\lambda)d_s}} = e^{-(\alpha_p(\lambda)-\alpha_s(\lambda))d} \tag{3.2}$$

where the thickness is forced to be equal and the reflection coefficient γ can be considered non dependent on the dopant concentration. This latter in fact is related to the change of the refractive index, that remains constant within experimental errors.
From the ratio in Eq. 3.2 it is possible to extract the absorbance $A = A_s/A_p = \log_{10}(T_p/T_s)$ and the absorption coefficient $\alpha_{Fe^{2+}}$ relative to the doped sample:

$$\alpha_{Fe^{2+}}(\lambda) = \alpha_p(\lambda) - \alpha_s(\lambda) = \frac{A}{d \ln 10} \tag{3.3}$$

For small concentrations of dopant, the previous expression can be written as a linear dependence on the donors concentration $[Fe^{2+}]$:

$$\alpha_{Fe^{2+}}(\lambda) = s_{Fe^{2+}}(\lambda)[Fe^{2+}] \tag{3.4}$$

where the proportionality constant $s_{Fe^{2+}}(\lambda)$ is the cross section of donor ions at λ wavelength. The value given by Berben in [37] for the cross section is $(3.95 \pm 0.08) \cdot 10^{-18}$ cm^2 for $\lambda = 532$ nm.
Fig. 3.2 shows the absorption spectra for three different y-cut sample, whose identification name is reported in the next section.

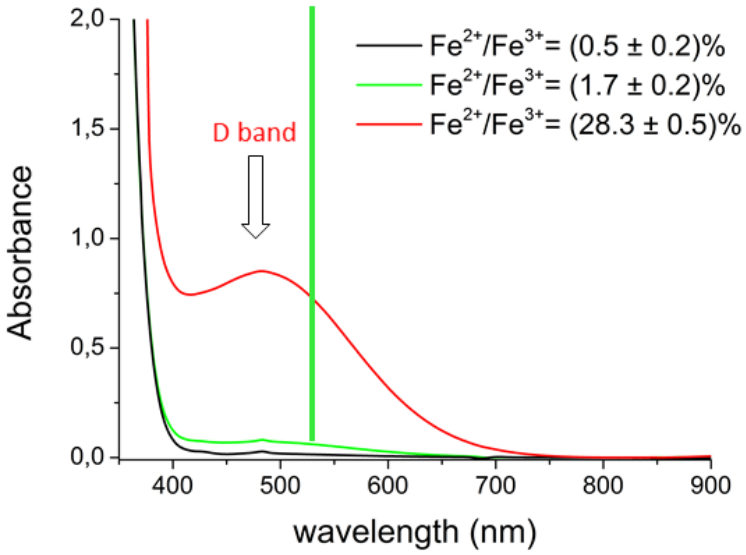

Figure 3.2: Optical absorption spectra of y-cut sample 151.18 (green), 151.21 (black) and 155.4 (red). The green vertical line indicates the 532.0 nm wavelength of the diode laser exploited for the optowetting characterization.

The band indicated in figure is the D band related to the amount of Fe^{2+} and it is more intense for the most reduced sample, as expected from theory.

3.4 Sample Nomenclature

During the whole thesis period several y-cut and z-cut Fe:$LiNbO_3$ samples were used in order to find the best conditions for an active droplets' control.

3.4.1 Y-cut Samples

Bulk y-cut samples produced by the $LiNbO_3$ group have been used for preliminary tests.
They are exploited to verify the behaviour of pendant droplets in response to laser spot illumination of the substrate and prove that its final position after fall on the surface is along the $\hat{z}$-axis.
In Tab. 3.1 the most relevant properties for each sample are presented: the doping degree[1] and the reduction degree, calculated for 532 nm wavelength. It is important to stress that all these samples have the same doping degree but an increasing ratio between iron in Fe^{2+} state and Fe^{3+} state.

Sample	Doping [% mol]	Reduction Degree [%]
151.18	0.1	0.5 ± 0.2
151.21	0.1	1.7 ± 0.2
155.4	0.1	28.3 ± 0.5

Table 3.1: List of y-cut samples with their identification numbers, doping degree, reduction degree and thickness.

3.4.2 Z-cut Samples

Bulk z-cut samples produced by $LiNbO_3$ and by Crystal Technology are also used, in particular for dynamic droplets' tests.
In Tab. 3.2 the most relevant properties for each sample are presented: the doping degree and the reduction degree, calculated for 532 nm wavelength. Also these samples have the same doping degree as the y-cut samples and the commercial z-cut sample is the most reduced.

Sample	Doping [% mol]	Reduction Degree [%]
154.5	0.1	9.9 ± 0.6
Commercial z-cut	0.1	32.4 ± 0.5

Table 3.2: List of z-cut samples with their identification numbers, doping degree, reduction degree and thickness.

[1] Doping degree is measured in molar percentage [% mol] of Fe ions: 1 % mol corresponds to $(18.8 \pm 0.1) \cdot 10^{19}$ at/cm^3.

(a) 151.18 y-cut

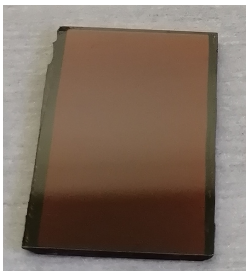

(b) 155.4 y-cut

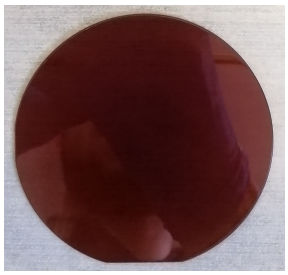

(c) Commercial z-cut

Figure 3.3: Photos of some Lithium Niobate samples.

3.5 Sample Functionalization: Hydrophobic Coatings

In order to detect the change in the wettability upon illumination by laser, the surface of $LiNbO_3$ samples is made hydrophobic by different coatings. The bare $LiNbO_3$ surface is in fact hydrophilic and water drops make a contact angle $\theta \approx 60°$. Therefore, after illumination, photovoltaic effect would lead a not appreciable variation of the contact angle.
Two different functionalizations have been used during the whole work: *(i)* Parafilm® for static contact angle evaluation and *(ii)* LIS of OTS impregnated with silicone oil for investigating the sliding of droplets on tilted samples.

3.5.1 Parafilm

Parafilm® is a semi-transparent film composed of a blend of waxes and polyolefins (C_nH_{2n}) that results to be thermoplastic, remarkable for its ductility and malleability, with a melting point at 60°C. It is commonly used in laboratory for sealing of vessels like beakers, Petri dishes or cuvettes and in microfludics is applicable on several devices. It is a hydrophobic material and a water droplet deposited on it forms a contact angle of $117° \pm 2°$.
To apply Parafilm on samples, opportunely cleaned with organic solvents (ethanol and acetone), it is extended and pressed on the $LiNbO_3$ surface, avoiding the formation of air bubbles or scratches. The final thickness of the layer becomes of the order of a dozen of μm, much less than the original one of 0.13 mm. Then the sample is put on a hot-plate at about 90°C for 10-15 minutes, by taking care that the heating takes place slowly to prevent pyroelectric effect, that would damage the crystal. For this reason, a thick metallic holder is interposed between the sample and the plate to increase thermal inertia and slow down the increase of temperature. Once parafilm is partially melted, the heater is switched off and the $LiNbO_3$ crystal is left on the hot plate for at least 15-30 minutes to cool down. This procedure has been optimized during the thesis and guarantees no damage of the $LiNbO_3$ crystal by heating.

3.5.2 LIS: OTS and Silicone Oil

In order to perform dynamic tests of droplets' sliding, samples must be covered by LIS. Among all recipes to create LIS proposed in literature, the chosen one for this work is described in [38] and resulted to be the most suitable for the purpose. It involves the deposition of a hydrophobic coating of octadecyltrichlorosilane (OTS), impregnated with silicone oil to create an atomically flat surface. This kind of LIS is preferable with respect to fluorurate oils, already used in [35], because the latter ones can charge easily, since fluorine is highly electronegative and the charges created on the $LiNbO_3$ surface can repulse or attract the overlying oil.

OTS is an amphiphilic molecule, represented in Fig. 3.4, whose chemical formula is $C_{18}H_{37}Cl_3Si$, is able to form self-assembled monolayers (SAM) on oxidic substrates. It is constituted by a polar head group ($SiCl_3$–), that reacts and attaches to the surface, and a long-chain tail ($C_{18}H_{37}$–) composed of carbons and 2 hydrogens for each C atom (except for the last one of the chain, that has 3 neighbours H atoms).

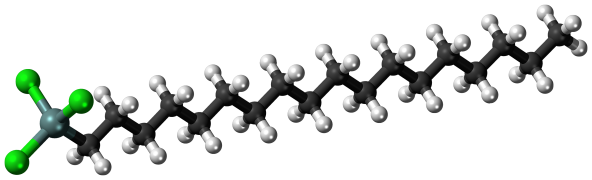

Figure 3.4: 3D representation of octadecyltrichlorosilane (OTS) molecule. Three Cl atoms (light green) attached to Si, forming the silane head, and the long chain composed of carbons (black) and hydrogens (white) are displayed in the sketch.

The recipe requires the immersion of cleaned substrates in 0.2% V/V solution of OTS in toluene for 20 min. Then, samples are dried in air in the fume-hood to let toluene evaporate (or, in alternative, heated at 90 °C for 30 min) and further cleaned in a bath of ethanol.
OTS is able to react with a glass surface, mostly made of silica (SiO_2), in the same way as with lithium niobate, because they both share the exposure of oxides, favourable to the chemical bond with the polar heads.

To obtain the final Liquid-Infused Surface, silicone oil must be deposited homogeneously on the sample. This operation can be performed by simply pipetting oil all over the surface or by using a dip-coater. In the first case, the oil in excess is removed by putting the specimen on nearly vertical position to facilitate the drainage. The final layer obtained is of about a dozen of μm, but it is clearly not very precise. The other method instead permits to control the formation of a layer with a given thickness. It consists in the immersion of the sample in a container full of oil and the emersion controlled by a motor that pulls the sample at a constant velocity to obtain a film of the desired thickness. Landau-Levich formula allows to calculate the withdrawal speed necessary for the oil layer above the sample to have a chosen thickness. The final thickness h_0 is estimated by:

$$h_0 = 0.94 \frac{(\eta U_0)^{2/3}}{\gamma_{LV}^{1/6} (\varrho_o g)^{1/2}}$$

where η and ϱ_o are the oil viscosity and density, U_0 is the withdrawal speed and γ_{LV} is the liquid-vapor surface tension [39].

For the preliminary tests on the evaluation of sliding velocity with systematic series, LIS is formed by depositing OTS on glass samples and impregnating it with silicone oils[2] of two different kinematic viscosities (100 cSt and 1000 cSt) by dip-coating. A final thickness of 6 μm, as obtained in [38], is achieved by a withdrawal speed of about 3.65 mm/min.
The underlying oil can in principle affect the velocity of droplets and so it is preferred to have the same thickness for all sequence of slips. However, for measurements on Fe:$LiNbO_3$ crystals there is no such a need to reach the precise thickness required for systematic tests and therefore oil is simply pipetted on the samples.

[2]The silicone oils used are Rhodorsil Oils 47 from Bluestar Silicones.

Chapter 4

Experimental Method

In this chapter the entire setup used for testing the sliding of droplets on illuminated Fe:$LiNbO_3$ samples is presented. A detailed description of the laser beam path and of the custom-made holders is given. The software used for data acquisition and processing and the procedures adopted for different series of measurements are specified.

4.1 Setup

The setup used in this work is composed of one part typical of optical measurements (Fig. 4.1a), that involves laser, filters and other components proper of an optical bench, and another one for microfluidics experiments (Fig. 4.1b).
The main components are listed and described in details in the following:

- Optical setup (Fig. 4.1a)
    1. Diode-pumped CW solid state laser (*MSL-FN-532-100mW*) at λ=532 nm wavelength, with beam diameter of about 2 mm and nominal power of 100 mW;
    2. Four mirrors to direct the laser beam;
    3. Turret with two series of circular optical filters to attenuate the power of the laser (Optical Densities from 0.1 to 3.7);
    4. A cylindrical lens to shape the gaussian beam into a strip along one direction. An holder let the cylindrical lens rotate around its centre.
- Microfluidic setup (Fig. 4.1b)
    1. Syringe pump, equipped with three possible needles with external diameters of 0.2, 0.7 and 1.27 mm. The pump is actuated by a dedicated controller (*World Precision Instruments Inc.*) to produce and deposit liquid drops of controlled volume on the substrate;
    2. White LED light (Phlox), as back light for the photographed object in order to obtain the contrast and brightness necessary for the images acquisition;
    3. Custom-made holder that permits to rotate the sample with respect to the vertical axis through a circular guide rail. It allows the laser beam to illuminate the sample from the bottom fixing the horizontal position. The holder system is mounted on a x-y-z micrometric translator, combined with a motorized x-y stage (with two controllers), to move the sample horizontally along a preferred path.

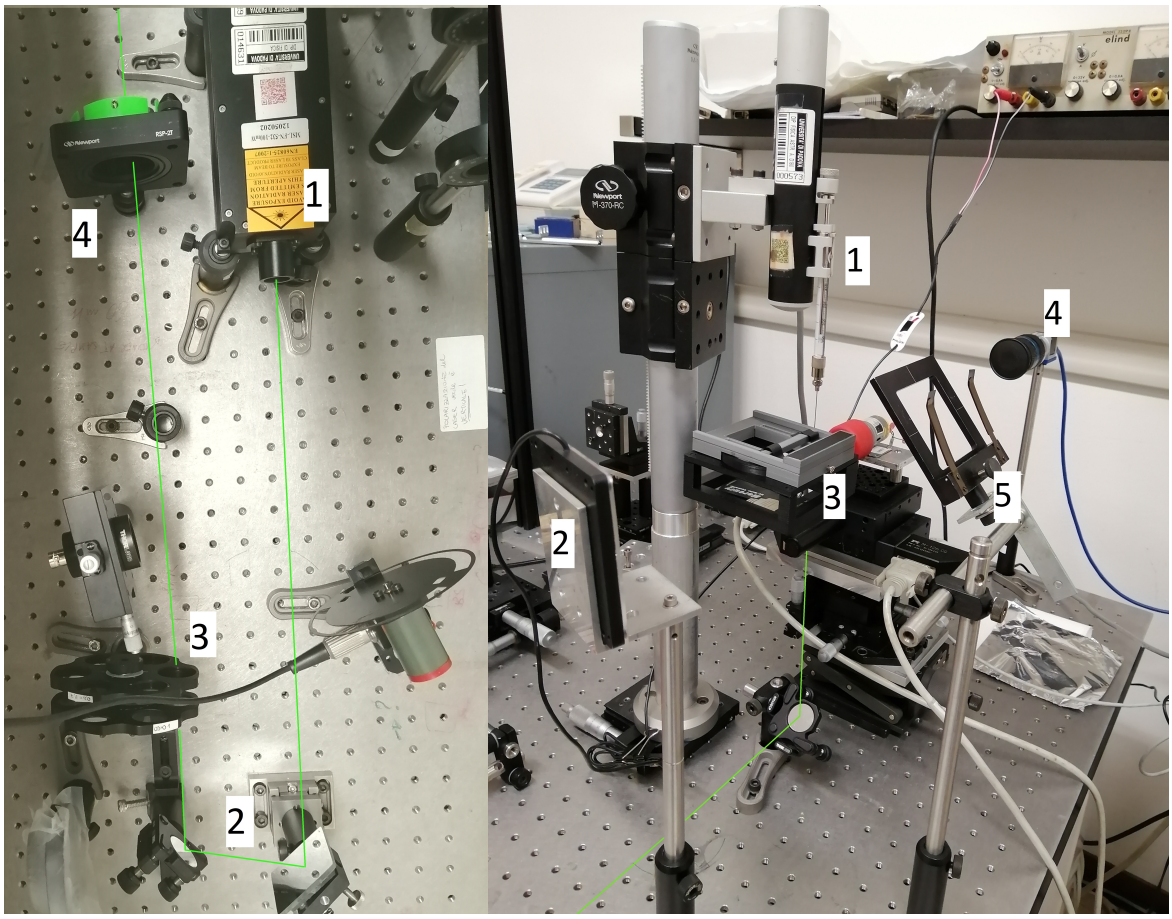

(a) Optic setup **(b)** Microfluidic setup

Figure 4.1: Photo of the entire experimental setup that comprises the optical part (a) and the apparatus for droplet slip (b).

4. CCD camera (*Basler acA1300-200um*) to record images and videos of sliding droplets on Fe:$LiNbO_3$ samples.

   A *Phantom v7.3* (by *Vision Research*) fast camera is instead used for preliminary sliding tests on glass samples with LIS.

   A telecentric objective (optical magnification 2x) with fixed focal length of 11 cm is mounted to monitor droplet profiles in order to measure the static contact angle after illumination on horizontal samples.

   A teleobjective (*Baumer Linos MeVis-C, 50 mm/f1.8*) with variable aperture (F 1.8-16) is used instead to record videos of sliding of droplets on tilted samples.

   An optical filter in front of the camera in order not to damage it. The filter absorbs the green light diffracted when the sample is illuminated by the laser beam.

5. An holder to fix the camera (or smartphone) to monitor droplet sliding.

4.1.1 Optical Path

The solid state laser emits a gaussian beam in continuous mode at the wavelength of λ=532 nm, with an effective power of about 70 mW. The path followed by the laser beam is schematized in Fig. 4.2. After exiting the laser, the beam is directed by two mirrors (M1 and M2), oriented at 45° with respect to the optical path to invert the direction by 180°. After M2 mirror, the beam passes through a turret mounting two filter wheels (F1), each with a series of neutral density filters with optical density (OD) varying from 0.1 to 3.7. They permit to attenuate the original laser power, and consequently the intensity, by a factor 10^x, where x is the OD value.
Then the light can encounter a cylindrical lens, which focuses the laser beam only in the direction parallel to the optical axis of the lens, whereas the beam size along the orthogonal direction is left unalterated. The lens is used to form a light strip on the Fe:$LiNbO_3$ sample, otherwise the gaussian beam creates a light spot with the same section of the original beam. The cylindrical lens can be rotated around its center thanks to the holder depicted in Fig. 4.3b: in this way it is possible to orient the main axis of the light strip along a desired direction on the Fe:$LiNbO_3$ substrate. The third mirror (M3) reflects the beam of 90° towards the last mirror (M4) that deflects it vertically. Therefore the Fe:$LiNbO_3$ sample, which is supported by the holder described in Fig. 4.3a, is illuminated perpendicularly from the bottom.

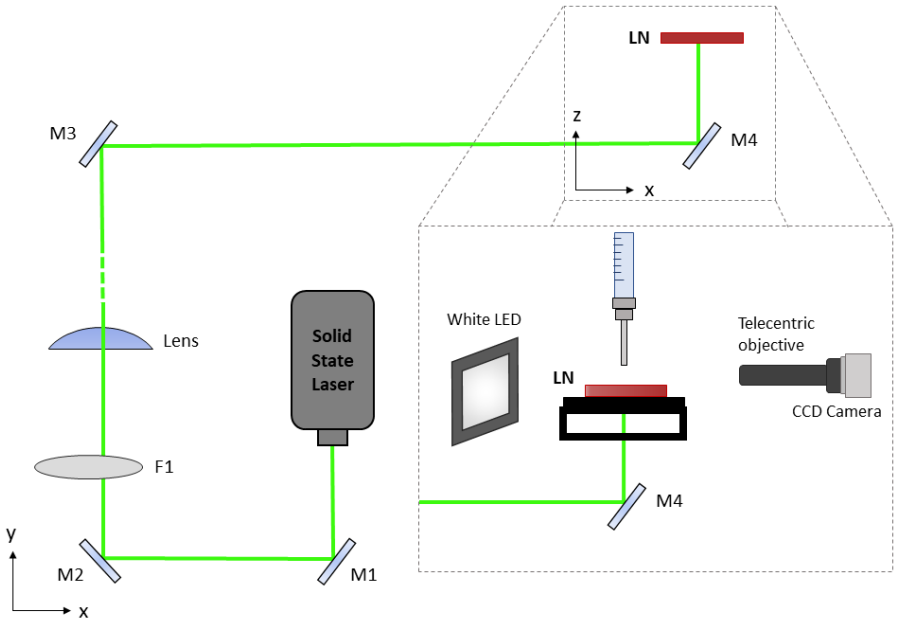

Figure 4.2: Sketch of the optical path.

4.1.2 Holders

Two holders designed with *Catia V5* (by *Dassault Systèmes*) and printed by *Prusa 3D printer* are added to the original setup used in [35], to facilitate the transcription of different patterns by the laser beam on the samples for final dynamic measurements. The 3D renderings of the holders are reported in Fig. 4.3.
The first one is customized to let the structure tilt with respect to the horizontal, so that the sample above the holder remains fixed at the chosen angle α. A motor, controllable manually or by an Arduino program, permits to reach this angle, by rotating clockwise or counter-clockwise

at the desired velocity. The upper part of the holder is able to rotate around the vertical axis by means of a circular guide rail. A rod fixable with two screws can be put above one extremity of the sample to block it. Moreover, a block at the end serves to make sure that, after tilting, the sample reaches the mechanic stop and cannot slide. A rectangular hole (70 x 38 mm) permits the laser to arrive from the bottom and illuminate the sample.
Another holder (see Fig. 4.3b) is designed for the cylindrical lens to let it rotate around its center. It is fixed onto a *Newport RSP-2T Rotation Mount* (for 2" optics) and has a central hole with a radius of 21.5 mm to let the laser pass through it.

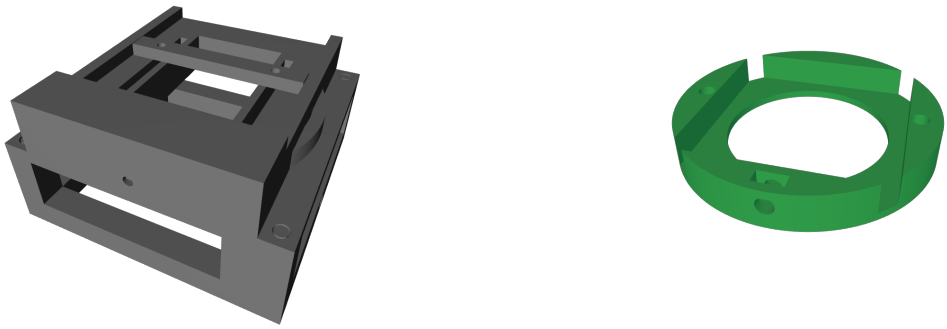

(a) Tilting holder **(b)** Lens holder

Figure 4.3: Schematic drawings of the two custom-made holders: the one used to tilt and rotate Fe:$LiNbO_3$ samples (a) and the one to rotate the cylindrical lens (b).

4.2 Acquisition System

Videos or single frames of droplets on the samples are acquired by the CCD camera or the fast camera connected to the PC and recorded by *Pylon Viewer* software at the desired frame rate and resolution. Systematic measurements of the profile of sessile droplets on the surface of Fe:$LiNbO_3$ samples are performed by a program written in *LabVIEW* that permits to calculate the contact angles. By selecting the desired region that contains the drop with a green rectangle, shown in Fig. 4.4, the program individuates a series of points that discriminates between two areas with a difference in contrast above a certain threshold. It then interpolates the profiles with a second-degree polynomial function. The parabolic fit is done for both left and right angle to verify the hysteresis. To evaluate distances and drop dimensions, a conversion from pixel to millimeters is done by recording a frame with an object of known dimensions.

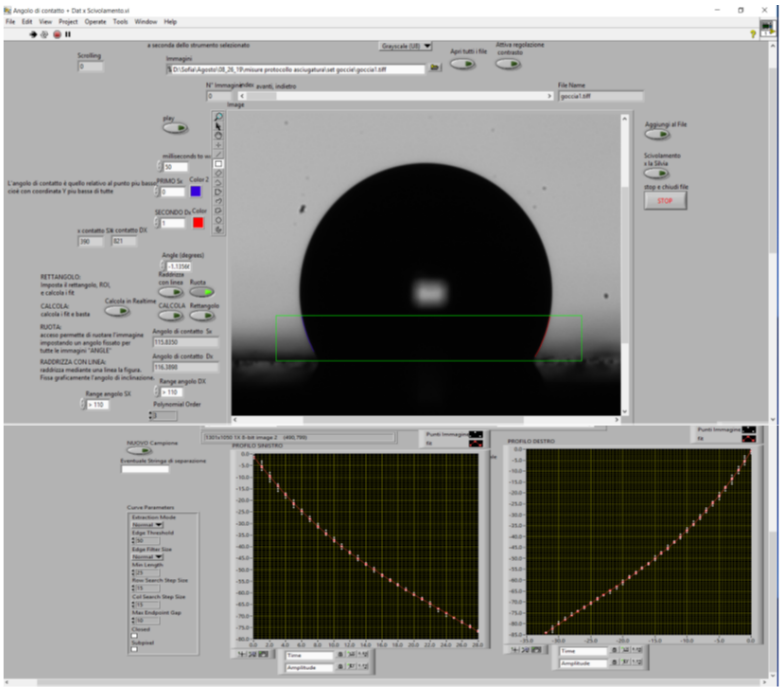

Figure 4.4: Screenshot of the LabVIEW program to compute the contact angles of droplets. The region of the frame delimited by the green rectangle contains the profile from which angles are measured. The values in degrees are obtained by interpolating with polynomial fits a selectable number of points in the profile.

4.3 Data Collection Protocol

In order to study the slippery behaviour of LIS and the interaction between water droplets and the electric fields created at the surface of illuminated lithium niobate substrates, several tests are made by depositing MilliQ water droplets on the surface. This kind of liquid is utilized during the entire work: the interest in water droplets arises from their wide range of applicability in different scientific areas, from chemistry to biology. After having verified the correct slip of droplets on tilted samples and the interaction between droplets and charge accumulations on lithium niobate substrates upon laser illumination, dynamic measurements of droplets' sliding on crystals with imprinted optical paths are performed.

The protocol followed in this work consists in several steps.

- **Sliding on Glass Samples coated with LIS**
  - Measurements to verify the behaviour of droplets' sliding on LIS, deposited on glass samples.
    Two different oil viscosities (100 and 1000 cSt) are compared by analyzing the slip of droplets with fixed volume (10 μl) on samples at different tilting angles.
  - Measurements to investigate the minimum volume at which sliding is reproducible.
    Sliding of droplets with different volumes are compared on glass sample impregnated with the same oil (100 cSt) tilted at fixed angle (45°).
- **Sliding on Fe:$LiNbO_3$ Samples coated with LIS**
  - Measurements to verify the independence upon the substrate of droplets' sliding on LIS.

A z-cut and a y-cut Fe:$LiNbO_3$ samples are used as substrate and the analysis of droplets' slip is made for different volumes and tilting angles.

- **Laser illumination on Fe:$LiNbO_3$ Samples**
  - Measurements to verify the accumulation of charges on Fe:$LiNbO_3$ samples by depositing droplets on the surface.

    Distances (heights) between the needle and the y-cut (or z-cut) sample at which droplets fall down affected by electric charges are measured for different times of laser illumination with fixed intensity.
  - Measurements to verify the effect on droplet fall of the laser intensity used to illuminate Fe:$LiNbO_3$ samples.

    Distances (heights) between the needle and the z-cut sample at which droplets fall down affected by electric charges are measured for fixed time of laser illumination with different intensities, obtained by using OD filters.
- **Dynamic Measurements on Fe:$LiNbO_3$ Samples**
  - Measurements on sliding of droplets with different volumes on y-cut (or z-cut) Fe:$LiNbO_3$ samples covered with LIS.

    Samples are tilted at different angles and illuminated for fixed time with a strip at different inclinations with respect to the horizontal axis.

Chapter 5

Results

In this chapter the results obtained from the analysis of optowetting measurements are presented and discussed. The first two sections are devoted to the study of the behaviour of LIS deposited on two different kinds of substrate: glass (in Sec. 5.1) and Fe:$LiNbO_3$ (in Sec. 5.2). Sec. 5.3 deals with the interaction between water droplets and light-induced electric field created on Fe:$LiNbO_3$ upon illumination, proved by measuring the drop heights of droplets, formed far from the charged surface. The relation between the intensity of the laser beam and the drop height is also investigated by using Optical Density filters, that reduce the laser power. In the last section the efficiency of light-induced virtual rails created on tilted Fe:$LiNbO_3$ samples are discussed, by monitoring the trajectories followed by moving droplets.

5.1 Sliding on Glass Samples with LIS

The first part of the thesis is dedicated to the study of Liquid-Infused Surfaces that will be exploited in this work both to reduce the friction coefficient of the investigated lithium niobate samples and to create an hydrophobic dielectric layer on their surface.
The efficiency of the lubricated surface, obtained by dip-coating, is proved by depositing with a pipette droplets with fixed volume ($V = 10\ \mu$l) along a tilted glass sample and by observing their motion, that should not be affected by pinning down the incline. The sliding velocities of water droplets are compared for two silicone oils of different kinematic viscosities: 1000 cSt and 100 cSt. Videos of the slips are recorded by the fast camera with high frame rate (from 50 to 250 fps) in order to distinguish any variation of velocity. For each sequence of frames recorded during the slip of one droplet (Fig. 5.1a), the custom-made LabVIEW program, presented in Sec. 4.2, permits to select a unique rectangle for all frames to individuate the contact angles of both the front and the rear of droplets down the incline. The position of the droplet at a certain time is determined by the front contact point. The reference position at time zero is determined by the front contact point of the droplet when it starts to be completely included in the selected area. A space-time plot for all droplets of one series (*i.e.* droplets measured in the same experimental conditions, such as fixed droplet volume and tilting angle of the substrate) is created, as shown in Fig. 5.1b. The selected rectangle used for image analysis is different for each droplet sliding and therefore the number of points reported in the graph can slightly differ for each data-sequence.

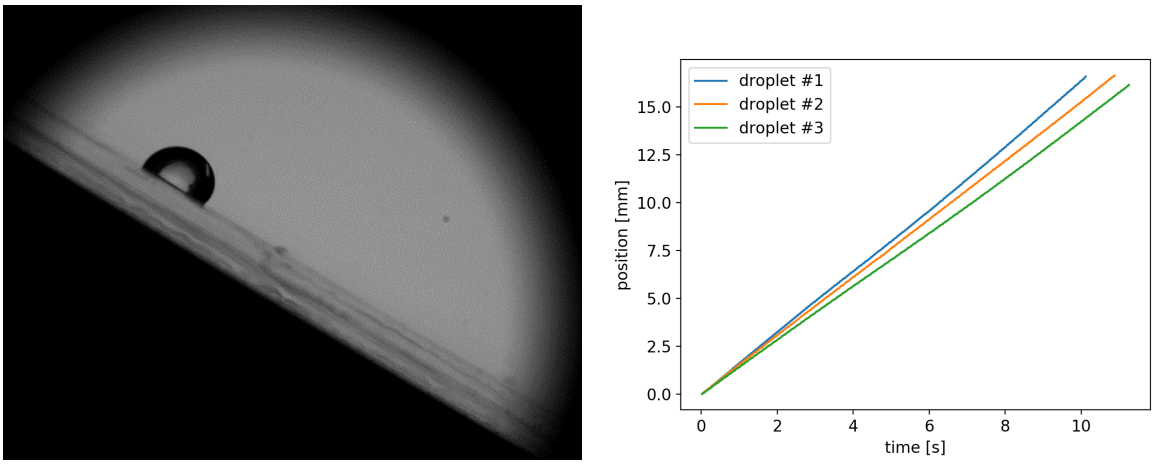

(a) Frame recorded by fast camera.

(b) Space-time plot for a series of droplets

Figure 5.1: Example of analysis of sliding droplets on LIS. On the left (a) a frame recorded for one droplet on LIS impregnated with 1000 cSt silicone oil on glass sample tilted at 30°. On the right (b) the plot for the position of three droplets as a function of time for that series.

A linear fit for each sequence of data is made and the value for the angular coefficient represents the velocity of a single droplet moving down the incline. The weighted average of the angular coefficients for all fits of the series gives the estimation of the sliding velocity at a given tilting angle of the sample.
For each value of oil viscosity, the sample is tilted at different angles α, as reported in Fig. 5.2a. The results are compared with those from [19] in Fig. 5.2b, in which the substrates made of micropillars covered by OTS are impregnated by silicone oils of 9.34 cP and 970 cP dynamic viscosity (correspondent to about 10 and 1000 cSt of kinematic viscosity) and BMIm[1].

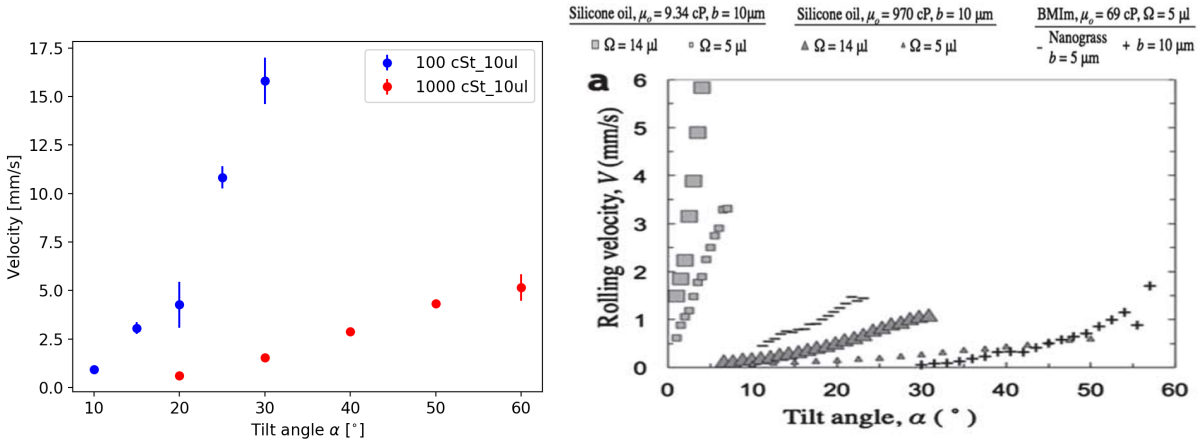

(a)

(b)

Figure 5.2: Droplet velocity vs. tilting angle. On the left (a) the two curves obtained from data with 100 cSt and 1000 cSt oil viscosities are plotted; on the right (b) results from [19] for different LIS are reported.

Sliding velocities obtained for similar experimental conditions are comparable: in fact, at fixed tilting angle of 30° our value for 1000 cSt oil and 10 μl droplet and their value for 970 cP oil

[1]It is an ionic liquid (1-butyl-3-methylimidazolium bis(trifluoromethylsulfonyl) imide). BMIm used in the paper has a viscosity of 69 cP.

with 14 μl droplet are very similar.
As expected, the more the sample is tilted the faster the droplets move down, because the component of the driving gravitational force, directly proportional to $\sin\alpha$, increases. It is found that the more viscous is the underlying oil, the more is the resistance to motion. This resistance is attributed to the drag force due to viscous shear, directly proportional to the dynamic viscosity μ_o of the oil.
The characteristic behaviour of LIS is verified by analyzing the trend of the Capillary number Ca, dependent on the sliding velocity v of the water droplet, as a function of the Bond number, defined respectively as:

$$Ca = \frac{\mu_w v}{\gamma} \quad \text{and} \quad Bo = \frac{\varrho g V^{2/3}}{\gamma} \tag{5.1}$$

where μ_w, γ and ϱ are the dynamic viscosity, surface tension and density of water.
To extract the relation between these two parameters, the rate of change of gravitational potential energy as the droplet moves down is balanced with the total rate of energy dissipation due to contact line pinning and viscous effects. The viscous dissipation derives from the effects within the droplet, the oil beneath it and the wetting ridge near the three-phase contact line. The thickness h_{film} of the lubricating oil (of 6 μm) and the height h_{cm} of the centre of mass of the droplet above the solid surface are both much smaller than the base radius R_b of the droplet. By considering this, the potential energy is primarily consumed by viscous dissipation in the wetting ridge around the base of the rolling droplet.
After some approximations [19], the relation found is:[2]:

$$Bo(\sin\alpha - \sin\alpha^*) \propto Ca\frac{\mu_o}{\mu_w} \tag{5.2}$$

In Fig. 5.3 a comparison between the results from this work and the one obtained in [19] is made.

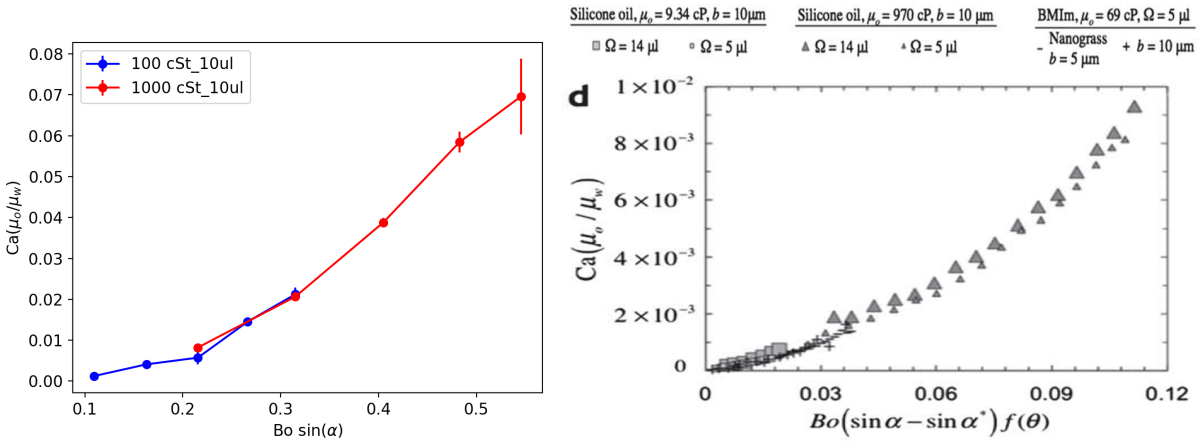

(a) (b)

Figure 5.3: Capillary number vs. Bond number. On the left (a) the two curves obtained from data with 100 cSt and 1000 cSt oil viscosities are plotted; on the right (b) results from [19] for different LIS are reported.

[2]In the first member there should be a factor $f(\theta)$ that relates the ideal spherical cap shape of the droplet with the R_b base radius, dependent on the contact angle θ with the surface, defined as:

$$f(\theta) = V^{1/3}/R_b = [(\pi/3)(2+\cos\theta)(1-\cos\theta)^2/\sin^3\theta]^{1/3}$$

It is worthy to note that the values of Capillary number calculated for the series with both oil viscosities overlap for Bond numbers in the range 0.2-0.3. Moreover, the comparison made with data from [19] in Fig. 5.3 shows that for all kinds of LIS the Capillary number (opportunely normalized by viscosities) follows the same behaviour, with a superlinear increase of the Capillary number with the Bonding one. This suggests that LIS used in this work exhibit the behaviour expected from literature. Since the LIS used in [19] are different, values in abscissas have different ranges depending on the critical sliding angle α^*, that in our case is much bigger.

The behaviour of our LIS is then compared with the ones obtained from the same recipe that are found in literature. In order to do so, the velocity for fixed droplet volume (10 μl) and tilting angle ($\alpha = 20°$) calculated for the two oil viscosities are compared with the ones from [38].
It is found that velocities from our work agree very well with the same trend of data in [38] and with the fitted curve obtained from theoretical model (red line in Fig. 5.4).

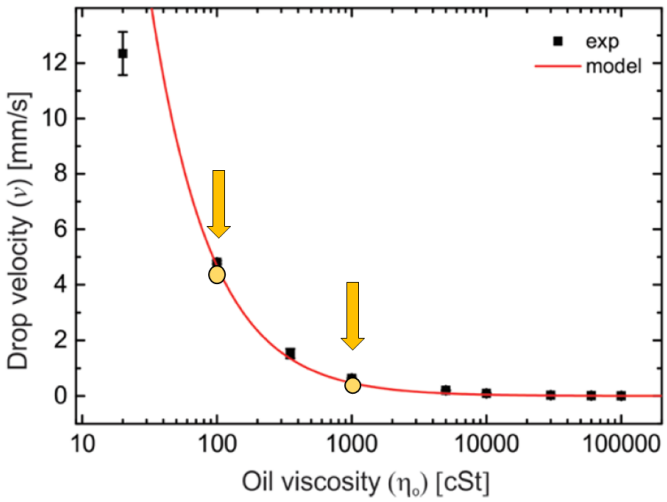

Figure 5.4: Droplet velocity vs. oil viscosity. Yellow big circles (indicated with arrows) are two velocities computed for 10 μl droplets on samples tilted at 20° on LIS with 100 cSt and 1000 cSt silicone oils obtained in this thesis, while black points are data from [38]. The solid red line corresponds to the fitted curve of the theoretical model discussed in the same paper.

Another series of droplet sliding on glass sample impregnated with 100 cSt silicone oil is made for different drop volumes V, in order to investigate the minimum volume that guarantees reproducible data where the pinning is not determinant. The tilting angle of the glass substrate is kept fixed at 45°. For large volumes (from 10 μl to 5 μl), barely affected by pinning, only five droplets are analyzed, while for small volumes (2-3 μl) ten droplets are tested. Even if the pinning is more significant at small volumes, velocities of consecutive droplets are very similar, as shown in Fig. 5.5a for 3 μl volume. Nevertheless, a re-impregnation after 10-15 droplets is recommended to have reproducible data. As expected, by increasing the dimension of the drop, gravity force increases and so the motion down the incline is faster, as seen in Fig. 5.5b.

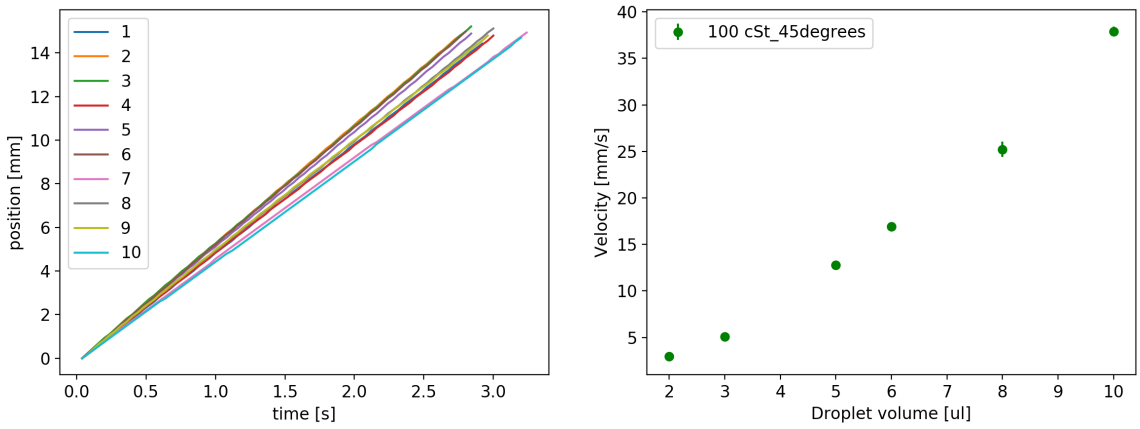

(a) (b)

Figure 5.5: Droplet velocity vs. droplet volume. On the left (a) the space-time plot for 3 μl droplets at 45° is reported, while on the right (b) average velocities are plotted as a function of droplet volumes.

Finally, the dependence of the Capillary number on the Bond number, that is proportional to the droplet volume as $V^{2/3}$, is compared with the two curves obtained by fixing the droplet volume and varying the tilting angle of the substrate.

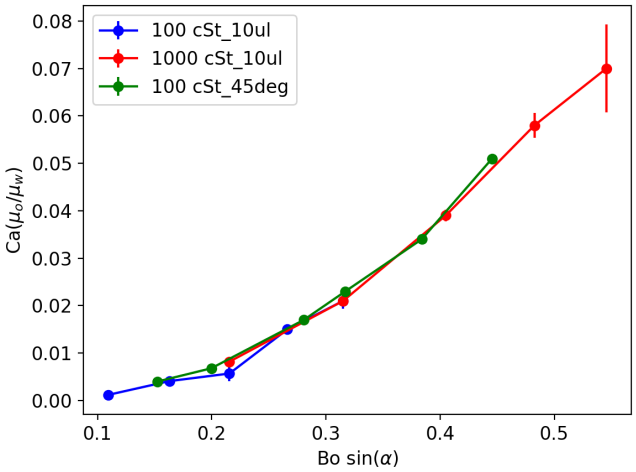

Figure 5.6: Capillary number vs Bond number for the three systematic series on glass sample. The trend for 10 μl on 100 cSt silicone oil is reported in blue, the trend for 10 μl on 1000 cSt silicone oil in red and the last measures by changing droplet volumes in green.

Fig. 5.6 shows that the three curves overlap as expected from literature ([38]), and thus the reproducibility of this kind of LIS is furtherly proved.

5.2 Sliding on Fe:LiNbO$_3$ Samples with LIS

The previous tests of droplets' behaviour on glass samples are repeated also on Fe:LiNbO$_3$ samples covered with the same LIS. For this purpose, a z-cut and y-cut crystals are used. The dimension of droplets and the tilting angles are chosen to be the smallest ones that ensure a reproducible downward velocity for many consecutive droplets, reducing pinning. A small size would permit an easier manipulation of the droplet by the optical patterns after sample illumination, and so it would be preferable for the last part of the work. Ten consecutive sliding droplets are examined for each kind of series for both z-cut and y-cut samples.

For both z-cut and y-cut samples the investigated parameters are:

- 3 μl volume, 45° tilting angle
- 5 μl volume, 45° tilting angle
- 5 μl (z-cut) and 3 μl (y-cut) volume, 60° tilting angle

Examples of space-time plots for two different series on z-cut are reported in Fig. 5.7.

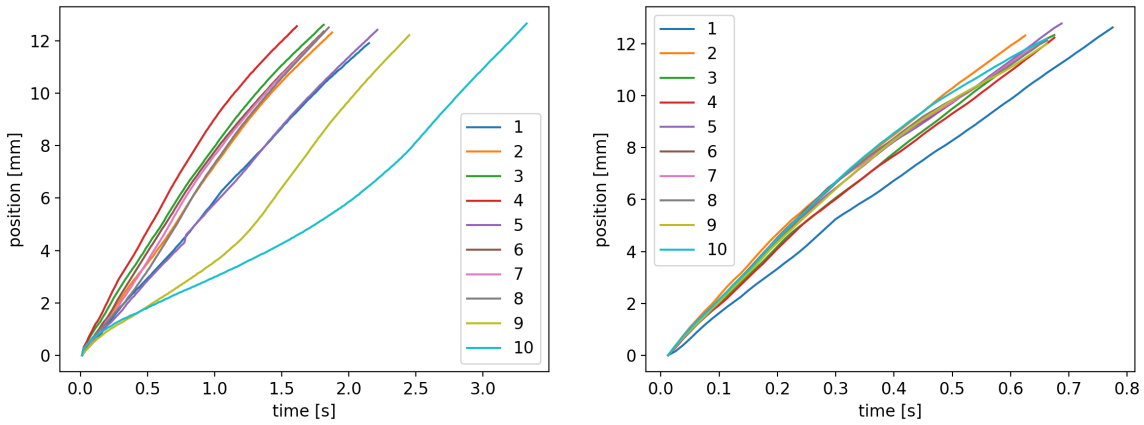

(a) 3 μl droplet, 45° tilting angle

(b) 5 μl droplet, 60° tilting angle

Figure 5.7: Space-time diagram for droplets sliding on z-cut sample with LIS.

It is evident that 3 μl droplets (in Fig. 5.7a) do not slide with constant velocity. The departure from linear behaviour is even more evident for the last two droplets of the series. This can be attributed to a non-homogeneity of LIS, since the lubricant oil is pipetted over the surface, realizing a deposition less controlled with respect to one obtained by dip-coating discussed in the previous chapter. For larger droplet volumes and/or tilting angles the problem is overcome, as shown in Fig. 5.7b. However, in this case the first droplet is slower with respect to the subsequent ones. This is probably due to the fact that it is more subjected to drag force, whereas the subsequent droplets benefit from the removal of excess oil made by the first falling drop, like in a sort of "wake effect".
On y-cut sample tilted at 45°, 30 droplets with 5 μl are deposited to determine the maximum number of droplets that ensure a correct slide with no re-impregnation needed. As it is possible to notice in Fig. 5.8, after about 15-20 droplets the velocities start to decrease while after 25-30 droplets the motion is no more linear. Therefore, the surface must be re-impregnated after 10-15 slips.

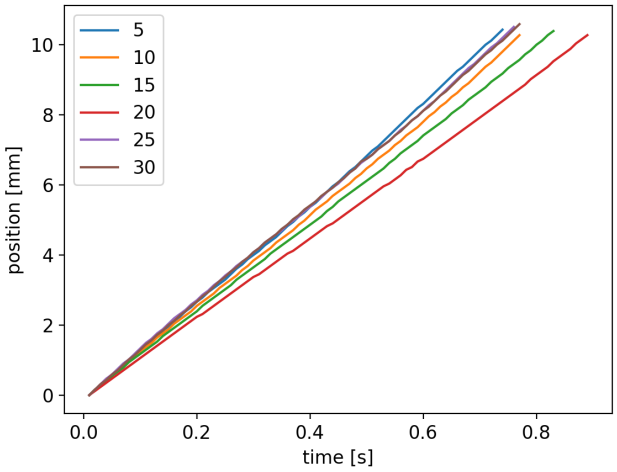

(a) 5 μl droplet, 45° tilt angle

Figure 5.8: Space-time diagram for droplets sliding on y-cut sample with LIS.

The LIS seems to be less efficient when deposited on lithium niobate than on glass. However, it is probably due to the fact that the deposition of oil over the sample was done by pipetting. Dip-coater was not used because less practical and more time consuming. This method has led to less precise and homogeneous deposition and this has remarkable effect on sliding, in particular for small drop volumes.
Fig. 5.9 shows that the trends for Capillary number as function of Bond number obtained on lithium niobate and glass substrates covered with the same LIS follow the same curve, as expected from literature.

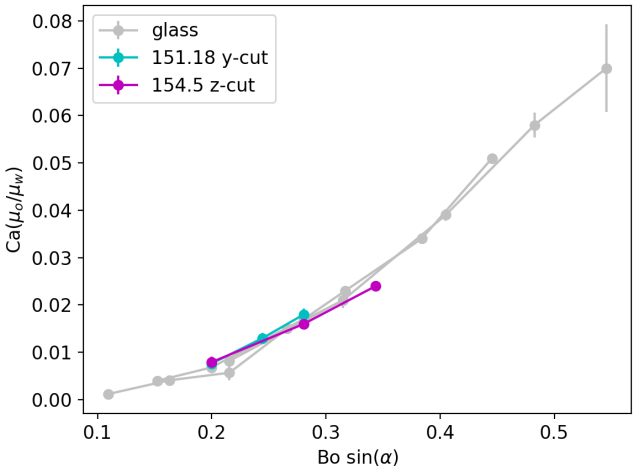

Figure 5.9: Capillary number vs Bond number reporting all data taken on Fe:LiNbO$_3$ samples. The trends on 151.18 y-cut sample are reported in cyan, the ones on 154.5 z-cut sample in magenta. The three previous series on glass sample are reported in silver.

Therefore, after having proved that the LIS behaves as expected, independently on the substrate, from now on the LIS will be used as coating for Fe:LiNbO$_3$ samples and the focus of the work will be shift to the photovoltaic effect of lithium niobate and the possibility to exploit this phenomenon to manipulate droplets on Fe:LiNbO$_3$ surface.

5.3 Laser illumination on Fe:$LiNbO_3$ Samples

The photovoltaic effect on Fe:$LiNbO_3$ crystals can be investigated by observing the behaviour of droplets subjected to charges accumulated at the surface by proper light illumination.
If a droplet is hanging on a needle at a certain distance above the illuminated sample, it will experience three forces (see Fig. 5.10): the gravitational force F_g, the capillary force F_c and the force F_e due to the light-induced charge accumulations present at the surface of the lithium niobate crystal. When approaching the substrate, the droplet starts to be affected by the charges on the crystal surface and elongates. When the capillary tension is no more able to overcome the force exerted by the light-induced charge accumulations and the gravity, the droplet falls down and touches the surface of the Fe:$LiNbO_3$ sample, reaching a contact angle that is lower than the one formed without illumination. The condition for the droplet to fall down is given by the inequality:

$$F_e + F_g > F_c \approx \gamma l \tag{5.3}$$

where γ is the water surface tension (with respect to air) and l is the circumference of the section of the needle. To reduce as much as possible the effect of gravity, droplets are formed on the needle with small volumes so that F_g is not the main contribution of the downward force.
The presence of a hydrophobic layer provided by the LIS should inhibit the compensation of photovoltaic charges on Fe:$LiNbO_3$ surface by the liquid droplet. Beside this, the hydrophobic layer permits to achieve a significant difference in the contact angle between illuminated areas and dark regions, far greater than the one starting from the hydrophilic bare crystal surface.

When the needle is positioned above the center of the gaussian beam that illuminates a z-cut sample, droplets fall down vertically on the charged spot, as shown in Fig. 5.10. Photos reported in Fig. 5.10c and Fig. 5.10d refer to a droplet affected by charges formed after 20 seconds of laser illumination, attenuated by an OD 0.5 filter, on z-cut sample with Parafilm. Even if the droplet is attracted by charges present on lithium niobate, the contact angle results to be greater than 90° because the illumination time is not long enough to produce a considerable charge density and consequently an appreciable change in wettability.

On y-cut (or x-cut) samples the distribution of charges is splitted on the two opposed sides along the $\hat{z}$-axis, at the borders of the illuminated spot, as depicted in Fig. 2.5. In these samples, if the needle is put above a point that does not coincide perfectly with the center of the illumination spot, the pendant droplet is attracted towards the nearest border (Fig. 5.11). Since in y-cut samples the amount of charges in the peripheral area of the spot is much less than the one obtained on z-cut sample (where on the contrary the charges accumulates in all the illuminated area), it will be necessary a longer time to have the same effect. Photos reported in Fig. 5.11c and Fig. 5.11d refer to a droplet affected by charges formed after 60 seconds of illumination on y-cut sample. The crystal is positioned with the $\hat{z}$-axis from left to right in the image and for this reason the droplet is attracted towards a side on the focus plane. The side in which the droplet falls does not depend on the sign of charges present on the substrate, since depending on whether it is closer to $+\hat{z}$ or -$\hat{z}$ side, water will polarize consequently.

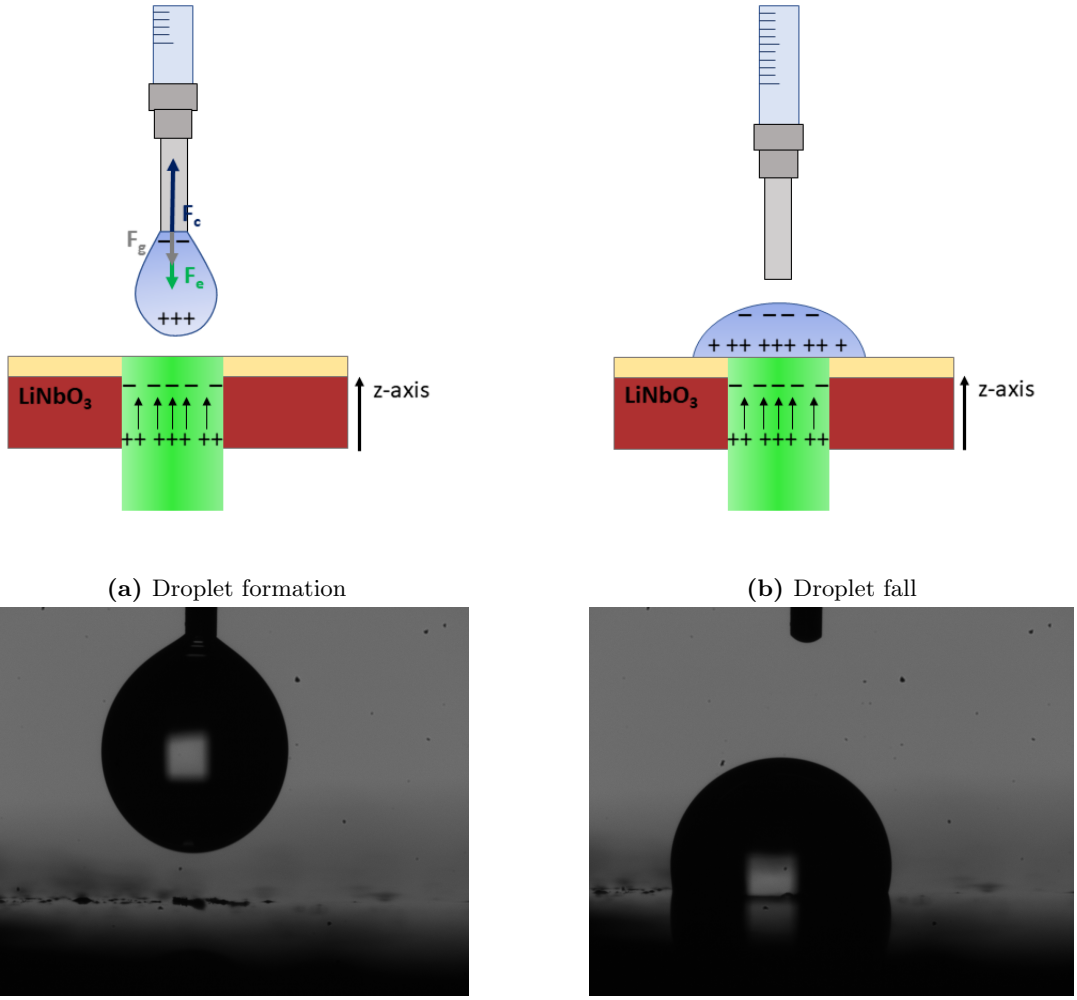

(a) Droplet formation

(b) Droplet fall

(c) Droplet formation

(d) Droplet fall

Figure 5.10: Photovoltaic effect on z-cut Lithium Niobate sample with Parafilm coating. Photos are taken for a 1 μl droplet on z-cut sample illuminated for 20 s with OD0.5 filter.

The different mechanisms of droplet fall observed in z-cut and y-cut samples can be explained in the frame of the dielectrophoretic force. This force acts on dielectric objects, like water drops, subjected to an inhomogeneous electric field.
The presence of an electric field distribution generates a dielectrophoretic (DEP) effect that affects the droplet polarization. The DEP force F on an approximately spherical water droplet in an inhomogeneous electric field is:

$$F = 2\pi r^3 \epsilon_w \frac{\sigma_w - \sigma_a}{\sigma_w + 2\sigma_a} \nabla(E^2) \tag{5.4}$$

where r is the droplet diameter, E is the electric field, ϵ_w is the dielectric constant of water and σ_w and σ_a are, respectively, the DC conductivities of water droplet and the surrounding medium (air) [40]. Since $\sigma_a \approx 10^{-9}$ S/m $\ll \sigma_w \approx 5 \cdot 10^{-6}$ S/m, the force is greater than zero, the droplet is said to exhibit "positive DEP" and experiences an attractive force toward regions of high electric field intensity.

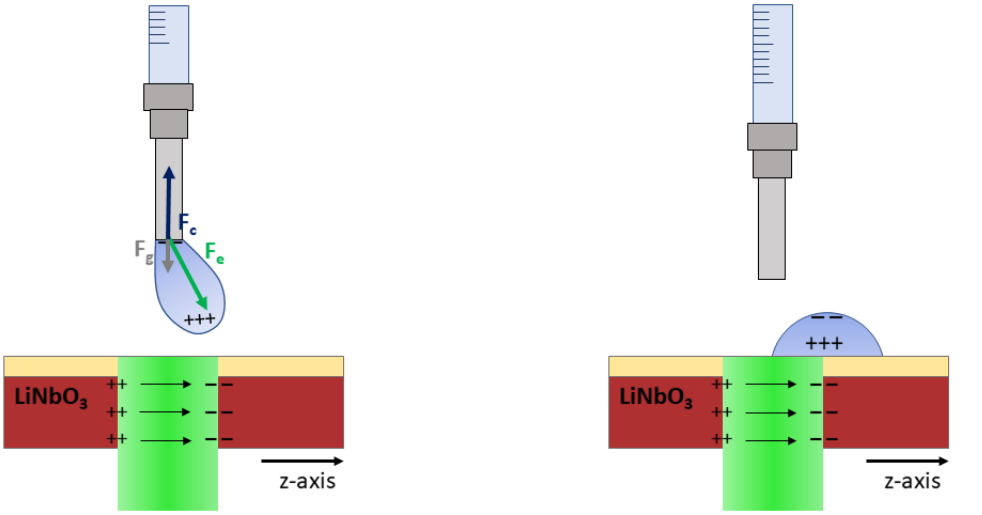

(a) Droplet formation

(b) Droplet fall

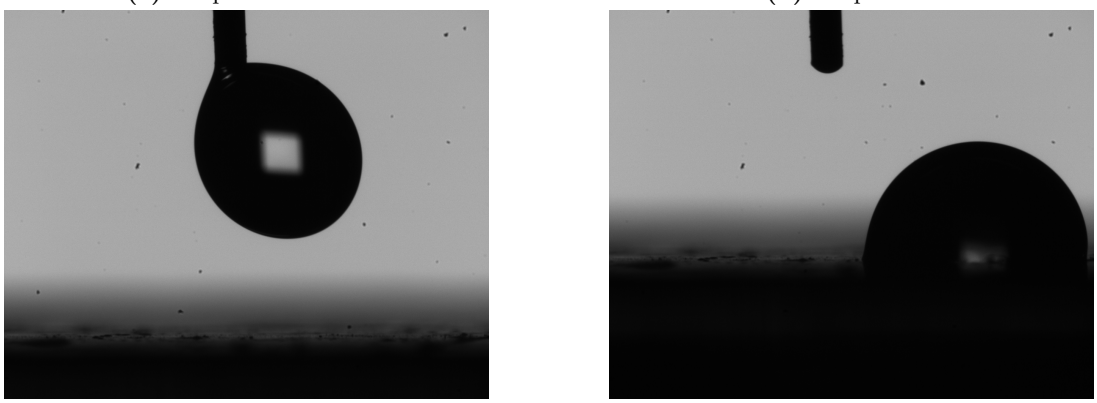

(c) Droplet formation

(d) Droplet fall

Figure 5.11: Photovoltaic effect on y-cut (or x-cut) Lithium Niobate sample. Photos are taken for a 1 μl droplet on 151.18 y-cut sample illuminated for 60 s without filters.

The separation of charges that occurs in the z-cut crystal can be compared to the two plates of a finite capacitor, with positive charge (positive potential) on -$\hat{z}$ side and a negative charge (negative potential) on +$\hat{z}$ side, as depicted in Fig. 5.12a. Conversely, on y-cut sample the two regions with different charge sign are set on both the main surfaces of the samples, as depicted in Fig. 5.11.

Fig. 5.12 illustrates Matlab simulations about charge and electric field distributions occurring in the case of a finite parallel-plate capacitor. As it is possible to notice, the fringing effects cannot be neglected and the intensity of the electric field is higher at the borders of the capacitor.

When a pendant droplet approaches a z-cut surface, it starts to be affected by DEP force from a long distance, where the field is already non-zero, as shown in Fig. 5.12b. The dielectric force attracts the droplet towards the areas where the intensity of the electric field is higher, that is at the borders of the illuminated region. However, in z-cut samples the dielectric force is symmetrically distributed with respect to the center of the light spot, therefore small misalignaments of the needle with respect to the center of the illuminated area do not significantly affect the droplet falls, whose final position is centered in almost all the case. Even if the needle is

not perfectly aligned with the center of the spot, the lateral gradient is not so appreciable and therefore the position with respect to the center is not so important.
On the contrary, above a y-cut crystal, the field is null apart from short distances from the sample. A small deviation from the center is affected near the surface by a considerable edge effect at the borders of the illuminated region. Hence, droplets' attraction towards one direction is highly dependent on the initial position of the needle with respect to the center of the spot.

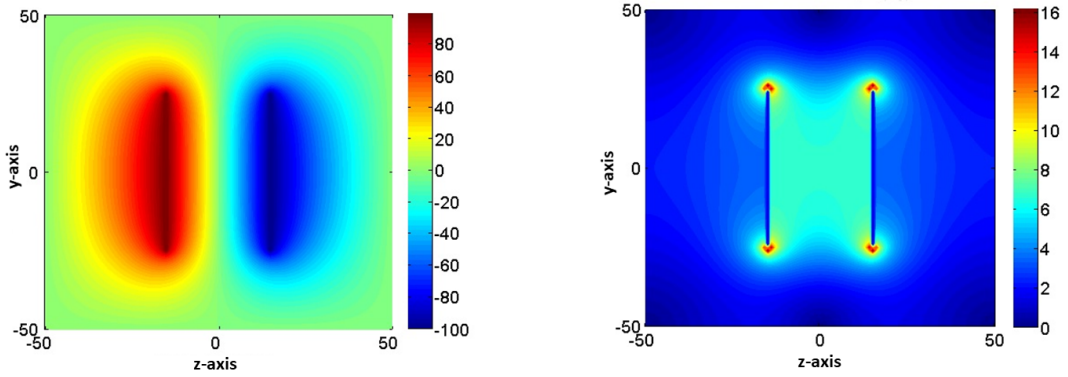

(a) Electric potential (a.u.)

(b) Electric field (a.u.)

Figure 5.12: Electric field and potential for a finite capacitor from Matlab simulation. On the left (a), the colormap from blue to red represents the negative and positive values for charges (and potentials) on $+\hat{z}$ and -$\hat{z}$ side. On the right (b) the electric field is strongly affected by the finite dimension of the capacitor.

5.3.1 Drop Height

Every kind of contact angle measurements for water droplets on illuminated Fe:$LiNbO_3$ samples is affected by the fact that drop is attracted by the surface charges and not simply deposited. After a long illumination time, droplets are influenced by the strong dielectric force exerted by the lithium niobate substrate, so they fall from a large distance, having a great velocity when touching the surface. The impact of the droplet onto the solid surface is strong and the final shape is flattened, thus resulting in a low contact angle that cannot be only attributed to optowetting phenomena. For droplets that fall from short distances, the contact angle is similar to the value registered when they are deposited directly on the surface, while increasing in height the contact angle can reach values lower than 90°.

Therefore, a more reliable method is chosen to evaluate the magnitude of the light-induced force, that is the height at which droplet falls from the needle. After the formation of 2 μl droplets on the needle at few centimeters from the surface, the sample is brought closer to the droplet till it falls. It is not possible to find the distance at which droplets starts to be affected by electric force and to oscillate and/or deform, since it depends also on the velocity of approach to the droplet, that cannot be the same for each test. Measurements are done with y-cut sample and the commercial z-cut sample for different laser illumination times, as reported in Fig. 5.13a. As a preliminary analysis, the curves are fitted with an exponential because the dependence of drop height on time reflects the behaviour of charge accumulation during illumination time, and the consequent formation of the light-induced electric field and corresponding dielectrophoretic force described in 2.8. The more the sample is illuminated, the more is the distance needle-crystal at which droplets start to fall.

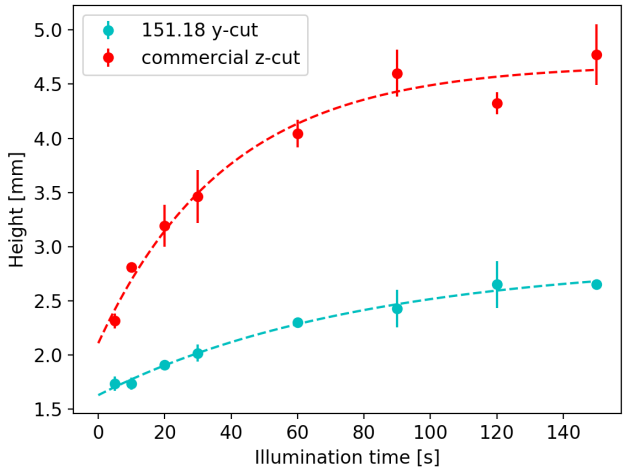

(a) Height at which suspended drops of 2 μl detached from the syringe needle vs. the illumination time of the substrate.

Sample	a [mm]	b [mm]	τ [s]
151.18 y-cut	1.6 ± 0.1	1.1 ± 0.1	51 ± 12
Commercial z-cut	2.0 ± 0.1	2.9 ± 0.1	45 ± 7

(b) Exponential fit parameters.

Figure 5.13: Drop height comparison between y-cut (151.18) and z-cut (commercial) samples, with exponential fit (a) and extrapolated parameters (b).

In order to evaluate the main parameters of the phenomenon, the exponential fit done for drop heights h has the form:

$$h = a + b(1 - e^{-t/\tau}) \tag{5.5}$$

where t is the illumination time. The parameter a represents the distance of the needle from the sample at which droplets touch the surface without falling down, while b is the difference between the maximum drop height, achieved when the Fe:$LiNbO_3$ crystal reaches the saturation, and the minimum height a. It is important to stress that the extrapolated a does not correspond exactly to the distance between the needle and the surface for a droplet deposited without previous illumination. The droplet elongates towards the region with charges; in the case of y-cut sample, the needle can get closer to the surface for small illumination times because of the oblique deformation. Thus, the obtained value for a for the z-cut sample overestimates the needle-surface distance for droplet contact without illuminating, while the one for the y-cut gives probably a result underestimated.
Despite the fact that the z-cut sample has a lower amount of Fe^{3+} and therefore a lower charge accumulation at its surface is expected, this sample is able to exert an attractive force on the droplet at larger distances with respect to the y-cut sample. This could be attributed to different distributions of the electric field outside the lithium niobate, which induces the arising of stronger DEP forces in the z-cut crystal, thus inducing the droplet fall also at higher height.
Concerning the time constants τ obtained from the fit, they significantly differ from the values expected by the photovoltaic theory. By considering the light intensity and the reduction degrees of the two samples, time constants of almost 60 s and 300 s are expected for the z-cut sample and the y-cut one, respectively. For the z-cut sample the agreement is very good, but this

is not the case for the y-cut crystal. However, this latter has an higher amount of Fe^{3+} and therefore stronger charge accumulations and electric field are expected to be created by laser illumination; moreover, the different distribution of the electric field intensity (see Fig. 5.12b) could significantly contribute to create a stronger gradient of the electric field than the z-cut samples, so that the resulting DEP force is able to affect the droplet fall already at shorter times than expected.
The advantage of z-cut sample is that much less time is needed for droplets to be affected by a considerable electric effect.

5.3.2 OD Filters Comparison

To evaluate the effect of laser intensity on the fall of droplets suspended to the syringe needle, Optical Density (OD) filters are used to attenuate the laser power. Measurements of the height at which 2 μl droplets detach from the needle in function of illumination time are performed. When filters are interposed between the beam and the commercial z-cut Fe:LiNbO$_3$ sample, times required to accumulate the same amount of charges on the surface increases, as expected from the theory on the photovoltaic effect.
Fig. 5.14a shows the data obtained with filters having OD equal to 0.1, 0.3 and 1.

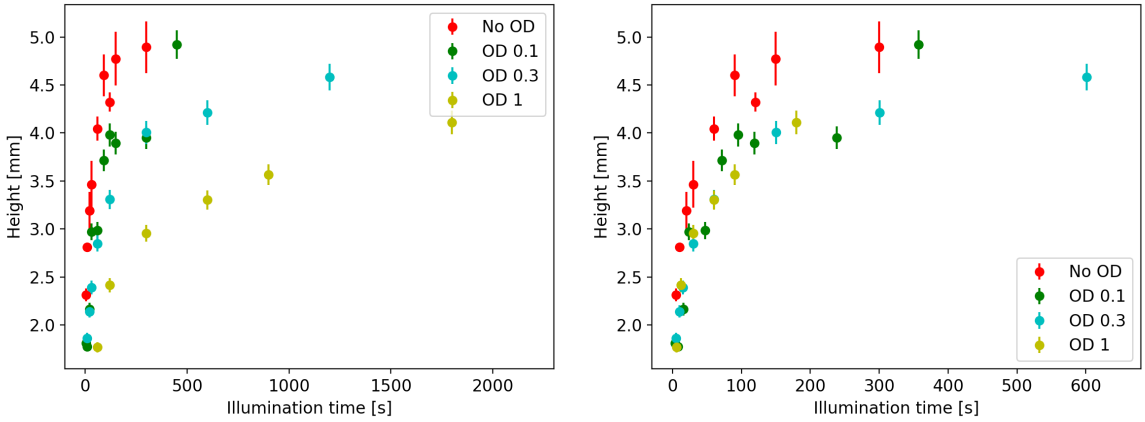

(a) Original data **(b)** Rescaled data

Figure 5.14: Comparison between drop height for illuminations of different intensities. In the right figure (b), times are rescaled by the attenuation factor: 1.2 for OD0.1, 2 for OD0.3 and 10 for OD1.

Filter	a [mm]	b [mm]	τ [s]
No filter	2.0 ± 0.1	2.9 ± 0.1	45 ± 7
OD0.1	1.6 ± 0.3	2.9 ± 0.3	75 ± 22
OD0.3	1.8 ± 0.1	2.6 ± 0.1	134 ± 23
OD1	1.8 ± 0.2	2.5 ± 0.2	588 ± 143

Table 5.1: Parameters of exponential fit on drop height in function of illumination time for commercial z-cut sample with different OD filters.

By lowering the intensity (by an attenuation factor 1.2, 2 and 10), τ increases in a proportional way. Fig. 5.14b shows that by rescaling the time with the attenuation factor all data collapse

on the same curve for short times, even if after the first linear part they have a less reproducible behaviour.
When the sample is illuminated by the laser beam, only the central part of the spot is affected by the intensity correspondent to the maximum of the gaussian. At first only in the central part the charge accumulation reaches the saturation value, then moving radially outwards all the illuminated points accumulate the maximum amount of free charges possible in greater times, proportionally to the light intensity distribution. By progressively decreasing the light power, the tails of the illuminated spot have not enough intensity to permit an appreciable charge accumulation at the border of the light spot in the timescale investigated in these measurements. Thus, because of this "threshold effect" for high OD values the total amount of charges at the surface is lower, which could explain the lower values of height reached at a given time with respect to experiments performed with lower optical density filters. In order to find the maximum height possible, further measurements should be performed with greater illumination times to be sure that the saturation is well reached and that for OD 0.3 and OD 1 gaussian tails are not cut, reducing the spot diameter.

5.4 Dynamic Measurements on Fe:$LiNbO_3$ Samples

The final part of the work is devoted to demonstrate that the laser beam can create charges on Fe:$LiNbO_3$ surface, acting as virtual electrode, that affect the motion of droplets while sliding down an incline. The efficiency of light illumination is verified by recording videos of sliding droplets that follow the imprinted line. Each test on y-cut sample follow a recipe that consists of the following steps:

1. placement of the sample on the holder horizontally and rotation about the vertical to obtain a strip at the desired angle ϕ with respect to horizontal axis;
2. illumination of the sample with the strip formed by the cylindrical lens for 5 minutes;
3. tilting of the sample through the motor to reach the desired tilting angle α;
4. formation of one droplet of given volume;
5. deposition of the droplet on top of the sample, along the vertical that intersects the strip;

For the first series of slips, y-cut sample is used: since it is a y-cut crystal, the density of charges induced on the surface is affected by the orientation of the strip with respect to $\hat{z}$-axis. Droplets of 3 μl volume are tested on the sample tilted at 45° and the strip forming angle of 60° and 75° with respect to the horizontal. Droplets of 5 μl volume are tested on the sample tilted at 30° and the strip forming angle of 45°, 60° and 75° with respect to the horizontal. For all these attempts droplets are affected by pinning at the strip or partial gliding with final pinning. By increasing the tilting angle at 45°, maintaining the strip at 60° and the volume of 5 μl, droplet follows the strip and than crosses it, as shown in the sequence of frames in Fig. 5.15.
On y-cut sample the evaluation of the trajectory of the droplet with respect to the charge is not trivial, since there are two distributions of charges placed at the borders of the strip. The first droplet can follow the line created by charges above the strip and then the second droplet should follow the second line of charges, but it can also be affected by the upper distribution if not completely discharged.

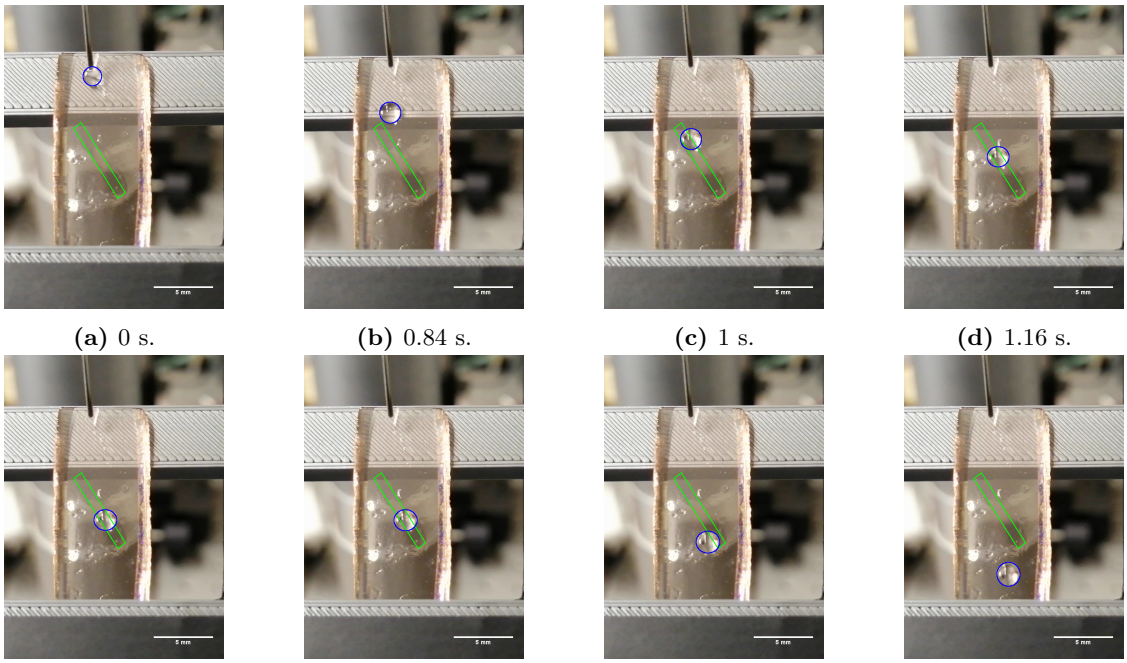

(a) 0 s. **(b)** 0.84 s. **(c)** 1 s. **(d)** 1.16 s.

(e) 1.33 s. **(f)** 1.5 s. **(g)** 1.66 s. **(h)** 1.84 s.

Figure 5.15: Sequence of frames of droplet sliding on 151.18 y-cut sample (5 μl droplet, 45° tilt angle, 60° strip angle, 5 minutes illumination). The droplet is highlighted with a blue contour, while the stripe region previously illuminated is represented with a green rectangle.

Therefore, to prevent such a problem the commercial z-cut sample is used as substrate for dynamic droplets control. Droplets with 9 μl volume are analyzed when sliding on the sample tilted by 30° and the strip at $\phi = 60°$ with respect to the horizontal, shown in the sequence of frames in Fig. 5.16. Differently from tests on y-cut sample, the z-cut sample is already tilted during laser illumination, that in this case takes 1 minute. The angle is lowered to decrease the velocity of the droplet and facilitate the electric force to compete with gravity force. It happens that the first droplet of a series follows the stripe completely, while the next one glides on the stripe only for a few millimeters and then falls along the vertical.

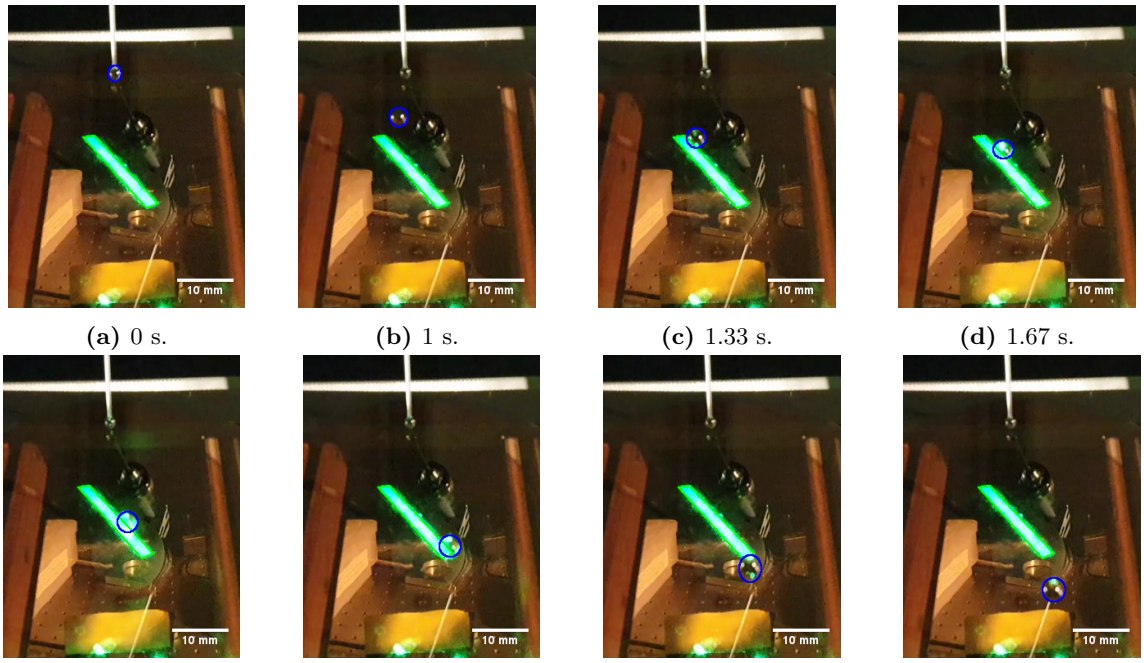

(a) 0 s. **(b)** 1 s. **(c)** 1.33 s. **(d)** 1.67 s.

(e) 2 s. **(f)** 2.33 s. **(g)** 2.84 s. **(h)** 3.5 s.

Figure 5.16: Sequence of frames of droplet sliding on commercial z-cut sample (9 μl droplet, 30° tilt angle, 60° strip angle, 1 minute illumination). The droplet is highlighted with a blue contour.

Chapter 6

Conclusions

This thesis work was devoted to the study of water microdroplets manipulation by means of laser illumination of a lithium niobate ($LiNbO_3$) substrate. This novel approach is based on the photovoltaic effect typical of this material, which permits to create strong charge accumulations and electric fields at the main faces of lithium niobate crystals simply via proper light illumination. To enhance the amount of charges that can be accumulated at the substrate surfaces, iron is used as dopant for $LiNbO_3$ crystals, since it is well known that this metal significantly enhances the photorefractive response of the material.
To favor the droplet motion, Fe:$LiNbO_3$ sample was functionalized with Liquid-Infused Surface (LIS) made of octadecyltrichlorosilane (OTS) and impregnated with silicone oil that permits to obtain an atomically flat hydrophobic surface. The performance of LIS was investigated on both glass and iron-doped lithium niobate samples with different cristallographic orientation to verify the independence of LIS performance on the kind of substrate. Sliding is found to be reproducible with the same velocity (within 10 %) for droplets with a volume greater than 3 μl. After 10-15 droplets the LIS should be re-impregnated to ensure the same velocity for consecutive measurements. Moreover, our results are found to be comparable with the ones obtained with the LIS found in literature.
The interaction between charges induced by the photovoltaic effect on lithium niobate and water droplets was also verified. Contact angle measurements were not so reliable since the final shape of the droplets on the surface is affected by the height from which they fall down when attracted by surface charges. For this reason, a better probe was found to be the drop height for different illumination times. For this kind of measurements LIS are not suitable, while solid surfaces with greater hysteresis are preferable to avoid droplet motion over them after the fall.
Drop heights measurements reveal that illuminated z-cut samples are able to attract droplets from larger distance with respect to y-cut samples, despite having a lower charge accumulation on their surface. This is probably due to the distribution of the electric field above the surface that in the former case creates stronger gradient and a greater DEP force. Much less illumination time is needed for droplets to be affected by a considerable electric effect and for this reason the z-cut sample is chosen as substrate for tests on active droplets' control.
Preliminary measurements on droplet sliding mechanisms were performed by creating light-induced virtual rails (stripe) and by varying the tilting of the Fe:$LiNbO_3$ substrate, the droplet volume and illumination time. It was found that droplets smaller than 3-5 μl are not suitable because are more subjected to pinning. Droplets of 9 μl volume on samples tilted at small angles (30°) can be reproducibly constrained to move along the desired stripe. Overall, the lower the sliding velocity, the easier the control of the trajectory.
In summary, the usefulness of the photovoltaic effect in attracting droplets and letting them move on the sample following desired paths is verified.

Further investigations are necessary to find the lower limit for illumination time, tilting angle for the sample and the stripe that permits droplets' gliding. Moreover, new tests can be performed to force droplets to follow paths different from a single line, *e.g.* by making a "flipper" or creating curve trajectories by pointwise illumination.

Chapter 7

Appendix

7.1 In-diffused Doped Fe:$LiNbO_3$ Samples

As a possibile alternative to bulk iron-doped samples, thermally *in-diffused* crystals can be considered, as described in Sec. 3.1. They are doped only on the surface by sputtering and then subjected to thermal treatments to promote the incorporation of dopants into the substrate.
As preliminary test an home-made sample was employed: the final shape for Fe dopant distribution resembles a semi-gaussian profile, whose maximum concentration at the surface, its mean-depth and the doping degree are reported in Tab. 7.1.

Sample	Doping [% mol]	Gaussian Dispersion [μm]	Reduction Degree [%]
210.6	0.8	2.9	4 ± 2

Table 7.1: Main properties of the in-diffused sample sample used for the preliminary test.

For each illumination time, two droplets with 1 μl volume are deposited. In fig. 7.1 the behaviour of the contact angle as function of illumination time is reported.

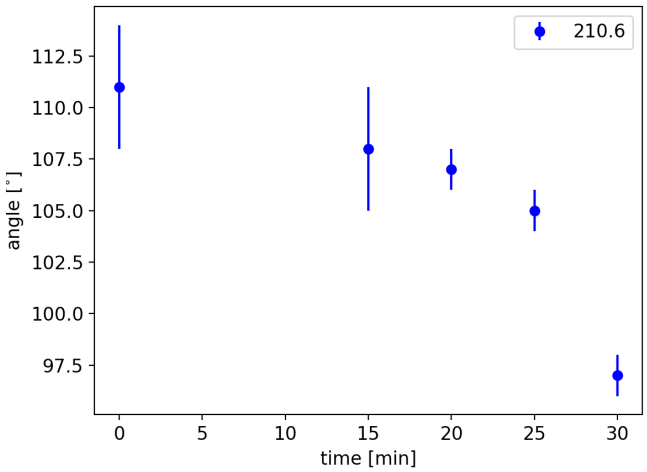

Figure 7.1: Contact angles for different illumination times on 210.6 in-diffused doped sample.

These contact angle measurements gives an idea of DEP effect on lithium niobate, but they are partly affected by the same problems described in Sec. 5.3.1 (even if the droplets detach when

they are almost in contact with the surface). To have a more reasonable comparison with data acquired with bulk samples, measurements with pendant drops have to be made.
The in-diffused samples would be preferable because of the lower cost and the home-made tailoring of their properties with the desired dispersion and doping degree. However, the first measurements showed that a lot of time was necessary to produce a remarkable optowetting effect, thus requiring further optimization steps. Future studies can be made on samples produced with a greater reduction degree to reduce consistently the illumination time for the photovoltaic effect and, possibly, a greater dopant concentration to strengthen the light-induced electric field.

Bibliography

[1] Whitesides G. M. The origins and the future of microfluidics. *Nature*, 442(28):368–373, 2006.

[2] Chen S. Tabeling P. *Introduction to Microfluidics*. OUP Oxford, 2005.

[3] Patankar N. A. Supernucleating surfaces for nucleate boiling and dropwise condensation heat transfer. *Soft Matter*, 6:1613–1620, 2010.

[4] Ma M. Mabry J.M. Mazzella S.A. Rutledge G.C. McKinley G.H. Cohen R.E. Tuteja A., Choi W. Designing superoleophobic surfaces. *Science*, 318(5856):1618–1622, 2007.

[5] Baret J.C. Mugele F. Electrowetting: from basics to applications. *Journal of Physics: Condensed Matter*, 17(28):705–774, 2005.

[6] Chen X. He Y Li Q. Li K.F. Wang Z. Hao G., Liu Y. Electrowetting on liquid-infused film (ewolf): Complete reversibility and controlled droplet oscillation suppression for fast optical imaging. *Scientific Reports*, 4:494–549, 2014.

[7] Schatz M.F. Garnier N., Grigoriev R.O. Optical manipulation of microscale fluid flow. *Physical Review Letters*, 91, 2003.

[8] Negran T.J. Glass A.M., Von der Linde D. High-voltage bulk photovoltaic effect and the photorefractive process in linbo3. *Applied Physics Letters*, 25(4):233–235, 1974.

[9] Wöhlecke M. Volk T. *Lithium Niobate: Defects, Photorefraction and Ferroelectric Switching*. Springer Berlin Heidelberg, 2008.

[10] Queré D. de Gennes P.G., Brochard-Wyart F. *Capillarity and Wetting Phenomena: Drops, Bubbles, Pearls, Waves*. Springer New York, 2013.

[11] Zhao H. Law K.Y. *Surface Wetting: Characterization, Contact Angle, and Fundamentals*. Springer Switzerland, 2016.

[12] Abu Jarad N. Soleymani L. Didar T.F. Villegas M., Zhang Y. Liquid-infused surfaces: A review of theory, design, and applications. *ACS Nano*, 13(8):8517–8536, 2019.

[13] Quéré D. Wetting and roughness. *Annual Review of Materials Research*, 38(1):71–99, 2008.

[14] Palgrave R.G. Parkin I.P. Self-cleaning coatings. *Journal of Material Chemistry*, 15:1689–1695, 2005.

[15] Federle W. Bohn H.F. Insect aquaplaning: Nepenthes pitcher plants capture prey with the peristome, a fully wettable water-lubricated anisotropic surface. *Proceedings of the National Academy of Sciences*, 101(39):14138–14143, 2004.

[16] Barthlott W. Koch K. Superhydrophobic and superhydrophilic plant surfaces: an inspiration for biomimetic materials. *Philosophical Transactions of the Royal Society A: Mathematical, Physical and Engineering Sciences*, 367:1487–1509, 2009.

[17] Tang S.K.Y. Smythe E.J. Hation B.D. Grinthal A. Aizenberg J. Wong T.-S., Kang S.H. Bioinspired self-repairing slippery surfaces with pressure-stable omniphobicity. *Nature*, 477:443–447, 2011.

[18] Queré D. Lafuma A. Superhydrophobic states. *Nature Materials*, 2(7):457–460, 2003.

[19] Anand S. Reza-Garduno E. Cohen R.E. McKinley G.H. Varanasi K.K. Smith J.D., Dhiman R. Droplet mobility on lubricant-impregnated surfaces. *Soft Matter*, 9:1772–1780, 2013.

[20] Nosonovsky M. Bhushan B. The rose petal effect and the modes of superhydrophobicity. *Philosophical transactions. Series A, Mathematical, physical, and engineering sciences*, 368(1929):4713–4728, 2010.

[21] van den Ende D. Mugele F., Duits M. Electrowetting: A versatile tool for drop manipulation, generation, and characterization. *Advances in Colloid and Interface Science*, 161(1):115–123, 2010.

[22] Lippmann G. Relations entre les phenomenes electriques et capillaries. *Annales de Chimie et de Physique*, 5:494–549, 1875.

[23] Berge B. Electrocapillarité et mouillage de films isolants par l'eau. *Comptes Rendus de L'Academie des Sciences Paris, Serie, II*, 317:157–163, 1993.

[24] Garimella S.V. Murthy J.Y. Annapragada S.R., Dash S. Dynamics of droplet motion under electrowetting actuation. *Langmuir*, 27(13):8198–8204, 2011.

[25] Gaylord T.K. Weis R.S. Lithium niobate: Summary of physical properties and crystal structure. *Applied Physics A*, 37(4):191–203, 1985.

[26] Betzler K. Schlarb U. Refractive indices of lithium niobate as a function of temperature, wavelength, and composition: A generalized fit. *Physical Review B*, 48:15613–15620, 1993.

[27] Panotopoulos G. Buse K. Luennemann M., Hartwig U. Electrooptic properties of lithium niobate crystals for extremely high external electric fields. *Applied Physics B*, 76(4):403–406, 2003.

[28] Lee T.C. Bernal E., Chen G.D. Low frequency electro-optic and dielectric constants of lithium niobate. *Physics Letters*, 21(3):259 – 260, 1966.

[29] Ferraro P. Grilli S. Dielectrophoretic trapping of suspended particles by selective pyroelectric effect in lithium niobate crystals. *Applied Physics Letters*, 92(23), 2008.

[30] Grilli S. Paturzo M. Vespini V. Ferraro P., Coppola S. Dispensing nano–pico droplets and liquid patterning by pyroelectrodynamic shooting. *Nature Nanotechnology*, 5(6):429–435, 2010.

[31] Huignard J.P. Günter P. *Photorefractive Materials and Their Applications 1*. Springer New York, 2006.

[32] Kukhtarev N.V. Kinetics of hologram recording and erasure in electrooptic crystals. *Pisma v Zhurnal Tekhnischeskoi Fiziki*, 2:1114–1119, 1976.

[33] Buse K. Peithmann K., Wiebrock A. Photorefractive properties of highly-doped lithium niobate crystals in the visible and near-infrared. *Applied Physics B*, 68(2):777–784, 1999.

[34] Saoncella S. *Optical control of droplet motion on Fe-doped lithium niobate crystals via photovoltaic effect*. Master Thesis, Università degli Studi di Padova, 2019.

[35] Paganini G. *Controllo del moto di gocce su cristalli di Fe:$LiNbO_3$ mediante fasci laser*. Tesi triennale, Università degli Studi di Padova, 2019.

[36] Ballmann A.A. Growth of piezoelectric and ferroelectric materials by the czochraiski technique. *Journal of the American Ceramic Society*, 48(2):112–113, 1965.

[37] Wevering S. Herth P. Imlau M. Woike T. Berben D., Buse K. Lifetime of small polarons in iron-doped lithium–niobate crystals. *Journal of Applied Physics*, 87(3):1034–1041, 2000.

[38] Barman J. Khare K. Sharma M., Roy P.K. Mobility of aqueous and binary mixture drops on lubricating fluid-coated slippery surfaces. *Langmuir*, 35(24):7672–7679, 2019.

[39] Brinker C.J. *Dip Coating*. Springer, Vienna, 2013.

[40] Clyde E. Stauffer. Highly reduced iron-doped lithium niobate for optoelectronic tweezers. *Applied Physics B*, 113:191–197, 2013.